

# Electron-magnon scattering in elementary ferromagnets from first principles: lifetime broadening and band anomalies

Mathias C. T. D. Müller, Stefan Blügel, and Christoph Friedrich  
*Peter Grünberg Institut and Institute for Advanced Simulation,  
 Forschungszentrum Jülich, 52425 Jülich, Germany*

We study the electron-magnon scattering in bulk Fe, Co, and Ni within the framework of many-body perturbation theory implemented in the full-potential linearized augmented-plane-wave method. To this end, a  $\mathbf{k}$ -dependent self-energy ( $GT$  self-energy) describing the scattering of electrons and magnons is constructed from the solution of a Bethe-Salpeter equation for the two-particle (electron-hole) Green function, in which single-particle Stoner and collective spin-wave excitations (magnons) are treated on the same footing. Partial self-consistency is achieved by the alignment of the chemical potentials. The resulting renormalized electronic band structures exhibit strong spin-dependent lifetime effects close to the Fermi energy, which are strongest in Fe. The renormalization can give rise to a loss of quasiparticle character close to the Fermi energy, which we attribute to electron scattering with spatially extended spin waves. This scattering is also responsible for dispersion anomalies in conduction bands of iron and for the formation of satellite bands in nickel. Furthermore, we find a band anomaly at a binding energy of 1.5 eV in iron, which results from a coupling of the quasihole with single-particle excitations that form a peak in the Stoner continuum. This band anomaly was recently observed in photoemission experiments. On the theory side, we show that the contribution of the Goldstone mode to the  $GT$  self-energy is expected to (nearly) vanish in the long-wavelength limit. We also present an in-depth discussion about the possible violation of causality when an incomplete subset of self-energy diagrams is chosen.

## I. INTRODUCTION

The interaction of electrons and spin excitations plays a fundamental role for a wide variety of phenomena. For example, spin-polarized currents depolarize due to their interaction with magnons [1], the characteristic temperature dependence of the tunneling magnetoresistance (TMR) [2] is determined by the electron scattering by magnons, and in nanospintronics the spin and charge currents that flow through nanostructures can be strongly affected by the electron-magnon interaction [3–6]. Moreover, it is speculated that the electron-magnon interaction is the origin of the superconductivity in Fe pnictides [7–10].

The elementary ferromagnets Fe, Co, and Ni are suitable model systems to study the electron-magnon interaction. They form a class of intermediately correlated materials in which localized  $d$  states close to the Fermi level are embedded in a free-electron-like band structure. While density-functional theory (DFT), employing either the local-spin-density (LSDA) or the generalized gradient approximation (GGA) to the exchange-correlation potential, is able to capture the ground-state properties of these materials, it fails to yield accurate excited-state properties. For example, the exchange splitting of these materials is often overestimated within DFT calculations. Nickel is an extreme case in that the exchange splitting is almost a factor of two too large.

A strongly spin-dependent band broadening is observed in angle-resolved [11] and two-photon photoemission experiments [12], which indicates that the electron-magnon interaction plays an important role in  $3d$  ferromagnets. In addition, recent angle-resolved photoemission spectroscopy (ARPES) experiments reveal pro-

nounced differences in the quasiparticle dispersion compared to DFT. ARPES measurements, for example, have exhibited anomalous kinks in the band dispersion of iron surface states [13] and nickel bulk states [14]. These kinks appear at binding energies much larger than what one would expect for a phonon-mediated band renormalization. It has been speculated that these band anomalies are a footprint of electron-magnon scattering because the energetic position of the kinks corresponds to typical magnon energies in the materials. We will later show that a similar band anomaly in iron, which was observed in ARPES spectra [15] at a comparatively large binding energy of 1.5 eV, can indeed be explained within our theory. (In this particular case, the theoretical prediction predated the experimental observation.)

The appearance of kinks in the electronic band dispersion and the strong band broadening of the quasiparticle peaks clearly go beyond the scope of a static mean-field theory such as DFT and calls for a genuine many-body description. One such method is the dynamical mean-field theory (DMFT), which maps the interacting many-body system onto an Anderson impurity model [16, 17]. DMFT relies on the choice of model parameters, the effective intra-atomic interaction parameters  $U$  and  $J$  as well as the intra- and inter-atomic hopping parameters. In applications to real materials, the latter are usually taken from a L(S)DA mean-field solution. An early implementation [18] of this LSDA+DMFT method showed that majority hole states are strongly damped in iron. This result has been confirmed by Grechnev *et al.* [19] who studied Fe, Co, and Ni with the same approach. They found a strong damping of the majority quasiparticle states and, in addition, a shallow satellite feature below the bottom of the  $d$  bands. A comparison of ARPES

spectra to LSDA+DMFT calculations [20–22] revealed that the agreement between experiment and theory is considerably improved with respect to LSDA, but still the linewidths and the effective masses tend to be underestimated compared to experiment. So far, no evidence of band dispersion anomalies has been found in the theoretical studies.

While allowing for an efficient treatment of many-body effects, the DMFT method suffers from some badly controlled approximations. Above all, the usage of the impurity model essentially amounts to neglecting the momentum dependence of the many-body scattering processes. Furthermore, the choice of the model parameters introduces an element of arbitrariness. Often they are fitted to experiment, which limits the predictive power of the method. Finally, since LSDA already contains the electron-electron interaction in an approximate way, it is necessary to apply a double-counting correction, for which no unique definition exists.

In this work, we employ an alternative description that avoids the usage of a model. The single-particle wave functions and propagators are allowed to extend over the whole (infinite) crystal. In this way, the momentum dependence is retained, and there is no need for model parameters nor a double-counting correction. Many-body perturbation theory (MBPT) is employed to construct an approximation to the electronic self-energy  $\Sigma(\mathbf{r}, \mathbf{r}'; \omega)$ . This effective scattering potential describes many-body exchange and correlation scattering processes that an electron or hole experiences as it propagates through a many-electron system. In other words, the self-energy connects the non-interacting mean-field system to the real interacting system. The solution of the Dyson equation then yields the single-particle Green function of the interacting system, and the imaginary part of which is directly related to the photoemission spectra [23].

The most popular approximation to the electronic self-energy is the *GW* approximation, which has been shown to yield accurate band structures for a wide range of materials. For example, it is known to have a strong effect on the band gaps of semiconductors and insulators [24], which are corrected from their (usually underestimated) DFT values towards experiment. The *GW* method has also been applied to the elementary ferromagnets, where it partly cures the shortcomings of LSDA. While the *3d* band width is typically overestimated in LSDA, the *GW* approximation applied to iron [25] and nickel [26, 27] yields results in better agreement to the experimental values [28–35]. The explicit electron-electron scattering of the *GW* self-energy gives rise to a lifetime broadening of the bands, which is, however, too small to explain the broadening seen in photoemission experiments, indicating that the *GW* self-energy misses some important scattering processes in these materials.

In this work, we derive from the Hedin equations [36] a first-principles self-energy approximation that describes the scattering of electrons and magnons. The Hedin equations are a set of integro-differential equations that,

if solved self-consistently, would yield, in principle, the exact self-energy for a many-electron system. A full self-consistent solution is not possible in practice, but the Hedin equations can be used to derive approximations to the self-energy. For example, the *GW* approximation results from a single cycle through the equations starting from  $\Sigma = 0$ . By iteration of the Hedin equations, one systematically generates more and more higher-order self-energy diagrams. In this way, we identify and select those scattering diagrams that are relevant for the coupling of electrons to many-body spin excitations. Then, summing these ladder diagrams to all orders in the interaction yields the *GT* approximation, where *T* stands for the magnon propagator, which describes the correlated motion of an electron-hole pair with opposite spins. It is shown that the lowest-order diagram of the *T* matrix is of third order in *W*, which renders double-counting corrections with *GW* unnecessary. The *GT* approximation has a similar mathematical form as the *GW* self-energy in that it is given by a product of the single-particle Green function *G* and the effective magnon propagator *T*. The implementation is, however, complicated by the fact that this *T* matrix is a four-point quantity: It depends on four points in space and results from a solution of a Bethe-Salpeter equation. A numerical implementation has been realized by employing a basis set of Wannier functions, which allow for an efficient truncation of the four-point quantity in real space. It should be noted that the present first-principles approach is based on a formulation at absolute zero, whereas DMFT approaches usually require the assumption of a finite electronic temperature.

The theoretical foundation of the *GT* self-energy is sketched in Sec. II. Section III discusses the self-energy contribution of electronic scattering with acoustic magnons (Goldstone mode) in the long-wavelength limit. The implementation of the *GT* self-energy within the SPEX code [27] is described in Sec. IV. The important topic of the violation of causality is discussed in detail in Sec. V. We analyze the many-body renormalization of the band structure of the bulk elementary ferromagnets iron, cobalt, and nickel in Sec. VI. The coupling of electrons to spin excitations leads to a pronounced spin-dependent lifetime broadening of the quasiparticle states. The lifetime broadening, which is particularly strong in iron, can lead to a complete loss of the quasiparticle character in certain energy regions of the electronic spectrum – with energy gaps appearing in electronic bands, effectively cutting them in two. Furthermore, we find a band anomaly at higher binding energy in iron, in agreement with a very recent ARPES study. Section VII gives a summary.

## II. THEORY

Our goal is to construct a self-energy that describes the many-body renormalization due to the scattering of electrons and magnons. Here, we should understand the term *magnon* to comprise not only the collective spin-wave ex-

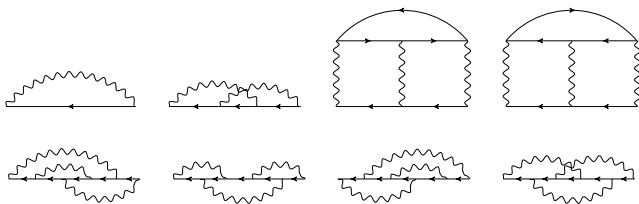


Figure 1: Feynman diagrams of the Hedin self-energy expansion up to the third order in the screened interaction  $W$ , which is denoted by a wiggly line. The Green function is denoted by an arrow.

citations but also the single-particle Stoner excitations, which provide a decoherence channel, through which the spin waves acquire a finite lifetime. In our formulation, the two types of spin excitations are treated on the same footing. They are intimately coupled to each other (two sides of the same coin) and cannot, as a matter of principle, be treated separately. In this sense, the self-energy will describe the dressing of a propagating particle (electron or hole) through the creation and annihilation of collective spin waves and single-particle Stoner excitations alike. We note that the spin-orbit coupling is neglected.

Figure 1 shows the self-energy expansion in Feynman diagrams up to third order in the screened interaction  $W$  as derived from the Hedin equations. Cutting the expansion at the first order yields the  $GW$  self-energy, an approximation commonly used in computational condensed-matter physics. Despite its success, however, it lacks a number of many-body scattering effects, for example, particle-particle (electron-electron and hole-hole) and electron-hole scattering as well as higher-order exchange processes. To account for these, the  $GW$  method has been combined [37–39] with the  $T$ -matrix theory, in which the self-energy is expanded in terms of infinitely many ladder diagrams, describing the correlated motion of two particles (electrons or holes). This  $GW+T$  approach is motivated phenomenologically: While  $GW$  describes the correlation of itinerant  $s$  and  $p$  states, the ladder diagrams account for correlation effects taking place in localized states. However, as the  $T$ -matrix self-energy contains the Hartree “tadpole” diagram and the direct term of the second Born approximation, which is also contained in the  $GW$  self-energy [62], a double-counting correction would be required in this approach [37].

Instead, we come back to the expansion shown in Fig. 1. Apart from the  $GW$  self-energy, this expansion consists of the second- and third-order screened exchange diagrams and two direct diagrams (the ones of third order in the first row) that also appear in the  $T$ -matrix approach. These two diagrams have the characteristic form of ladder diagrams where the rungs of the ladder correspond to the screened interaction and the rails correspond to single-particle Green functions. They describe the correlated motion of an electron-hole pair and a particle pair (electron-electron or hole-hole), respec-

tively. If the electron and hole are of opposite spins, the corresponding propagator can be seen as part of a solution of the Bethe-Salpeter equation (BSE) for the transverse magnetic response function [40–43]. The full BSE solution would comprise ladder diagrams of all orders, including the first and second as well as the infinitely many higher-order diagrams. For example, the collective spin-wave excitations arise from a resummation of ladder diagrams up to infinite order. Transversal spin waves are low-energy excitations (going down to zero energy for vanishing momentum in the absence of spin-orbit coupling). The corresponding self-energy diagrams are therefore expected to yield the principal low-energy scattering contribution in ferromagnets. The particle-particle diagrams, on the other hand, have been shown to be responsible for the appearance of satellite features, e.g., the 6 eV satellite in nickel [37]. The electron-hole diagrams without a spin flip (electron and hole have the same spin) couple to density and longitudinal spin fluctuations, which are of much higher energy (in the order of the plasma frequency) than the transversal spin waves. The other diagrams shown in Fig. 1 cannot describe a coupling to spin fluctuations because, in the absence of spin-orbit coupling, they have a single continuous Green-function line with a unique spin quantum number.

For these reasons, we have implemented the electron-hole self-energy ladder diagrams, starting at the third order as prescribed by the Hedin self-energy expansion. The summation is to all orders in  $W$  (the third-order diagram generates the fourth-order diagram in the next cycle of the Hedin equations and so on) but excludes the first- and second-order diagrams, which avoids the double-counting problem mentioned above. Iterating the Hedin equations thus yields, in a natural way, a combination of the  $GW$  and the  $T$ -matrix self-energy that is free from double-counting errors.

At this point, we should mention that an implementation starting from the third-order diagram was already considered in Ref. 37 but dismissed because the authors had realized that the renormalized Green function violated a causality condition: The imaginary part of the Green function showed an incorrect change of sign at large (absolute) energies. We observe the same behavior and discuss below in detail that the sign change is not a numerical artifact but, in fact, expected to occur for the presently chosen self-energy diagrams. However, we argue that this violation of causality can be accepted as the sign change is observed in an energy region, which is not in the focus of the present paper. In particular, it is expected that other self-energy diagrams, neglected in the present work, will play a more important role there and should eventually act to restore the correct sign.

From a physical point of view, the self-energy diagrams, which form what we call the  $GT$  self-energy in the following, describe the emission and re-absorption of magnons. Here, the magnons should again be understood to comprise both spin waves and Stoner excitations. In this sense, the  $T$  matrix can be viewed as an effective

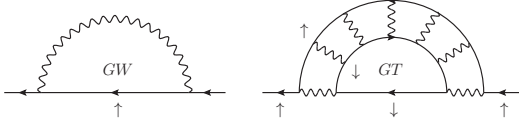


Figure 2:  $GT$  diagram (right) drawn to resemble the  $GW$  diagram (left). The  $T$  matrix is a magnon propagator. The  $GT$  self-energy thus describes the emission and re-absorption of magnons in much the same way as  $GW$  describes the corresponding processes for plasmons. Note that, after emission of the magnon, the spin of the propagating particle has flipped, since the magnon carries a total spin of unity.

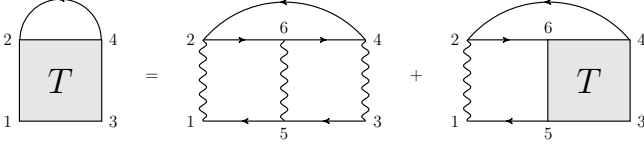


Figure 3: Feynman diagram of the electron-magnon self-energy in the ladder approximation. Notation as in Fig. 1. It is assumed that the Green functions that are solely connected by the screened interaction have opposite spins.

interaction that acts through the exchange of magnons in much the same way as  $W$  includes the exchange of plasmons. To illustrate this analogy, we represent the self-energy diagram in a way that resembles the  $GW$  diagram in Fig. 2. However, we will see that the  $T$  matrix is a much more complex quantity than  $W$  as it is a four-point function, i.e., it depends on four points in space (and time), whereas  $W$  is a two-point function.

The  $GT$  self-energy is expected to yield an important scattering channel for electrons in magnetic materials. We should mention already at this point that for the present study we omit the explicit evaluation of the  $GW$  self-energy for simplicity and employ a corrected LSDA solution instead. This solution is made to fulfill the Goldstone condition for the spin excitations and has been shown [44] to resemble the self-consistent solution obtained with the Coulomb-hole screened-exchange (COHSEX) self-energy, the static limit of  $GW$ , and to bring the exchange splittings closer to experiment.

The  $GT$  self-energy

$$\Sigma^\sigma(13) = -i \int d2 d4 T^{\sigma\sigma'}(12, 34) G^{\sigma'}(42) \quad (1)$$

with the spin indices  $\sigma$  and  $\sigma' = -\sigma$  is written in terms of the interacting time-ordered single-particle Green function  $G^\sigma$  and an electron-hole  $T$  matrix. We have used the short-hand notation  $1 = (\mathbf{r}_1, t_1)$ , and atomic units are used throughout. Figure 3 shows a representation in Feynman diagrams. In the ladder approximation, the multiple-scattering  $T$  matrix is the solution of the BSE

$$T^{\sigma\sigma'}(12, 34) = \int d5 d6 W(12) K^{\sigma\sigma'}(12, 56) \times \left\{ W(56) K^{\sigma\sigma'}(56, 34) W(34) + T^{\sigma\sigma'}(56, 34) \right\} \quad (2)$$

with the screened interaction  $W(12)$  in the random-phase approximation (RPA) and the free electron-hole pair propagator

$$K^{\sigma\sigma'}(12, 34) = iG^\sigma(13)G^{\sigma'}(42). \quad (3)$$

Equation (2) defines the  $T$  matrix to contain the ladder diagrams to all orders starting from the third order in  $W$ .

### III. GOLDSTONE CONTRIBUTION

As already mentioned, the  $T$  matrix is closely related to the transverse magnetic response function  $R^{+-}(12) = \delta m^+(1)/\delta B^+(2)$ , which gives the linear response of the spin density with respect to an externally applied circularly polarized magnetic  $B$  field. For simplicity, we omit “+” and “−” denoting the circular polarizations in the following. We now generalize the spin density to the spin density matrix  $m(12)$  and the magnetic field to a non-local field  $B(34)$ . Then, the four-point response function  $R(12, 34) = \delta m(12)/\delta B(34)$  can be written as the solution of a BSE (see, e.g., Ref. 43 [63]). In matrix notation, the solution reads  $R = -2(\mathbb{1} - KW)^{-1}K$  with the free electron-hole pair propagator of Eq. (3), which has poles at the energies of the unrenormalized Stoner excitations. The inverse  $(\mathbb{1} - KW)^{-1}$  renormalizes these Stoner excitations, but it also gives rise to the collective spin-wave modes. Without it, one would simply obtain  $-2K$ , the transverse magnetic response function of the non-interacting mean-field system.

An important special case is the limit  $\mathbf{k} \rightarrow \mathbf{0}$ . In this limit (and in the absence of spin-orbit coupling), a static  $B$  field that is orthogonal to the spin polarization is able to rotate the spins collectively towards the field direction even if  $B$  is infinitesimally small. This leads to a spin-wave delta peak in  $R$  at  $\mathbf{k} = \mathbf{0}$  and  $\omega = 0$ . For finite  $\mathbf{k}$ , the spin-wave dispersion can be shown [45] to be quadratic in  $k$ , which, in a more general sense, corresponds to the Goldstone mode expected to arise in the case of a spontaneously broken symmetry [46, 47] such as ferromagnetism. The delta peak at  $\omega = 0$  results from the infinite summation of ladder diagrams and will thus also appear in the  $T$  matrix, where it is likely to pose a numerical problem in the evaluation of the self-energy. Therefore, we discuss its contribution to Eq. (1) in the following.

As a first step, we have to characterize the Goldstone delta peak in a more detailed way. As already mentioned, an externally applied infinitesimal transversal  $B$  field can rotate the electron spins macroscopically. In order for this rotation to be rigid (collective rotation of the spins), the linear transversal change of the ground-state spin density matrix  $m(12)$  must be proportional to  $m(12)$  itself,  $\delta m \propto m$  (intercept theorem). Thus, integrating the response function  $R$  with the infinitesimal  $B$  field should give a finite response proportional to  $m$ . Conversely, the inverse of  $R$  should

have a vanishing eigenvalue with the eigenvector  $m$ , i.e.,  $(\mathbb{1} - KW)m = 0$ . We now sketch a proof that this is fulfilled if the Coulomb-hole screened-exchange (COHSEX) self-energy is taken as the starting point. For brevity, we use a simplified notation. The static COHSEX self-energy  $\Sigma^\sigma(12) = -W(12)n^\sigma(12) + \Sigma_c(1)\delta(12)$  with the density matrix  $n^\sigma(12)$  consists of the screened exchange (Hartree-Fock exchange potential with a statically screened Coulomb potential) and a static Coulomb-hole self-energy, which has the form of a local potential. When separating off the spin-independent part  $[(\Sigma^\uparrow + \Sigma^\downarrow)/2]$ , the remaining spin-dependent part can formally be interpreted as arising from a nonlocal magnetic field  $B(12) = -W(12)m(12)/2$ , which gives rise to the spin polarization in the COHSEX mean-field solution. Now we use the simple fact that rigidly rotating this  $B$  field will rotate the magnetization in the same way, implying the proportionalities  $\delta B \propto B$  and  $\delta m \propto m$  with  $\delta B/B = \delta m/m$ . With the magnetic response function  $-2K$  of the mean-field system, corresponding to the formula for  $R$  without the inverse, we can formulate this magnetic response as  $-2K\delta B = \delta m$  (in matrix notation), and, with the above relationship for  $\delta B$  and  $\delta m$ , we thus have  $-2KB = m$ . Then, inserting  $B = -Wm/2$  finally yields  $KWm = m$ . This proves that  $m$  is an eigenvector of  $\mathbb{1} - KW$  with vanishing eigenvalue, a claim that we have previously [44] substantiated with arguments of theoretical consistency. There is another more detailed proof, which is presented elsewhere [43].

To continue, we have to define a basis in which the quantities are to be expanded. We will later use a Wannier product basis, but, for the present purpose, it is easier to consider products of single-particle wave functions  $\{\varphi_{\mathbf{k}m}^\uparrow(1)\varphi_{\mathbf{k}'m'}^{\downarrow*}(2)\}$  as a basis, instead. The Goldstone condition  $KWm = m$  gives  $m$  as an eigenvector in this basis. With  $m(12) = n^\uparrow(12) - n^\downarrow(12)$  and

$$n^\sigma(12) = \frac{1}{N} \sum_{\mathbf{k}} \sum_m f_{\mathbf{k}m}^\sigma \varphi_{\mathbf{k}m}^\sigma(1) \varphi_{\mathbf{k}m}^{\sigma*}(2) \quad (4)$$

with the number  $N$  of  $\mathbf{k}$  points and the occupation numbers  $f_{\mathbf{k}m}^\sigma$ , we obtain after expansion of  $\varphi_{\mathbf{k}m}^\sigma(1)$  in terms of  $\{\varphi_{\mathbf{k}m'}^\sigma(1)\}$

$$m(12) = \frac{1}{N} \sum_{\mathbf{k}} \sum_{m,m'} (f_{\mathbf{k}m'}^\uparrow - f_{\mathbf{k}m}^\downarrow) \langle \varphi_{\mathbf{k}m}^\downarrow | \varphi_{\mathbf{k}m'}^\uparrow \rangle \varphi_{\mathbf{k}m}^\downarrow(1) \varphi_{\mathbf{k}m'}^{\uparrow*}(2). \quad (5)$$

According to this expression, we can immediately conclude (because of the factor  $f_{\mathbf{k}m'}^\uparrow - f_{\mathbf{k}m}^\downarrow$ ) that the nonzero eigenvector elements are those where one of the states  $(\mathbf{k}m \uparrow)$  or  $(\mathbf{k}m' \downarrow)$  is occupied and the other is unoccupied. If the spin-up and spin-down states are not too different from each other, we can also see that the combination  $(\mathbf{k}m \uparrow)$  occupied and  $(\mathbf{k}m' \downarrow)$  unoccupied gives a sizable contribution, while the other term is negligible (because of the small overlap).

These considerations are helpful in the discussion of

the Goldstone-mode contribution to the  $GT$  self-energy

$$\Sigma^\sigma(\omega) = -\frac{i}{2\pi} \int_{-\infty}^{\infty} T^{\sigma\sigma'}(\omega') G^{\sigma'}(\omega - \omega') d\omega', \quad (6)$$

here written in simplified notation and Fourier space. The frequency integral can be evaluated along a closed contour from  $-\infty$  to  $\infty$  and back to  $-\infty$  along an infinite semicircle in the upper or lower complex half-plane. The latter does not contribute because both the  $T$  matrix and the Green function behave asymptotically as  $\omega^{-1}$ . When writing  $G$  and  $T$  as sums over poles [e.g., see Eq. (11)], the contribution of any pair of poles can be evaluated with the residue theorem, and it vanishes unless the poles are both below or both above the real frequency axis (note the negative sign of  $\omega'$  in the Green function).

Let us consider the spin-down case first. The  $T^{\downarrow\uparrow}$  matrix has the Goldstone delta peak infinitesimally below the real frequency axis, so its contribution is proportional to  $1/(\omega - \epsilon_M + i\eta)$  with  $\epsilon_M = 0$ . Then, in the frequency convolution of Eq. (6), only the poles of the Green function that are also below the real axis contribute, which, according to Eq. (11), are those of the unoccupied states  $(\mathbf{k}m' \uparrow)$ , resulting in self-energy poles at  $\epsilon_{\mathbf{k}m'}^\uparrow + \epsilon_M = \epsilon_{\mathbf{k}m'}^\uparrow$ . According to Eq. (5) and the discussion thereafter, the unoccupied states  $(\mathbf{k}m' \uparrow)$  must be combined with occupied states  $(\mathbf{k}m \downarrow)$  to form the eigenvector of the  $T$  matrix that is related to the Goldstone peak. The corresponding eigenvector elements are exactly those that have been discussed above to be very small. Furthermore, because of the combination of states, only the self-energy matrix elements that couple occupied states can get a non-zero contribution from this eigenvector, for example, the diagonal element  $\Sigma_{\mathbf{k}m}^\downarrow(\omega) = \langle \varphi_{\mathbf{k}m}^\downarrow | \Sigma^\downarrow(\omega) | \varphi_{\mathbf{k}m}^\downarrow \rangle$ . The contribution would consist of poles located at frequencies larger than the Fermi energy, thus in an energy region that is less relevant for the renormalization of the occupied states  $(\mathbf{k}m \downarrow)$ . Analogous arguments apply to the spin-up case: The  $T^{\uparrow\downarrow}$  matrix has its Goldstone delta peak infinitesimally above the real-frequency axis. So, it is the Green-function poles related to the occupied states  $(\mathbf{k}m \downarrow)$  that now give rise to self-energy poles at  $\epsilon_{\mathbf{k}m}^\downarrow$ , the other poles do not contribute. These states have to be combined with the unoccupied states  $(\mathbf{k}m' \uparrow)$ —the same combination as before—to yield a contribution to the diagonal element  $\Sigma_{\mathbf{k}m'}^\uparrow(\omega) = \langle \varphi_{\mathbf{k}m'}^\uparrow | \Sigma^\uparrow(\omega) | \varphi_{\mathbf{k}m'}^\uparrow \rangle$  with poles at frequencies below the Fermi energy. Again, these poles do not play an important role for the renormalization of the unoccupied states  $(\mathbf{k}m' \uparrow)$ .

The Goldstone contribution to the  $GT$  self-energy is thus expected to be small. Of course, the spin-wave peaks at finite  $\mathbf{k}$  and  $\omega$  can contribute sizably to the self-energy, and we will see that these collective excitations can give rise to anomalies in the electronic band dispersions.

#### IV. IMPLEMENTATION

We have implemented the *GT* self-energy into the *GW* code SPEX [27]. The self-consistent DFT calculations are carried out with the FLEUR code [48]. Both codes rely on the all-electron full-potential linearized augmented-plane-wave method, which provides an accurate basis set for the representation of both the itinerant *s* and *p* states as well as the localized *d* states. Solving the BSE [Eq. (2)] leads to an infinite series of ladder diagrams. This series appears also in the diagrammatic expansion of the transverse magnetic response function (then starting from the first order in *W*), for which we reported an implementation in the Refs. 41-44. The implementation exploits the fact that the Hamiltonian is not explicitly time dependent. In addition, the RPA screened interaction  $W(\mathbf{r}, \mathbf{r}'; \omega)$  is approximated by its static limit  $W(\mathbf{r}, \mathbf{r}') = W(\mathbf{r}, \mathbf{r}'; 0)$ . As a result, the self-energy [Eq. (1)] involves only a single frequency integration. Furthermore, we restrict ourselves to calculating only the diagonal elements  $\Sigma_{\mathbf{q}m}^\sigma = \langle \varphi_{\mathbf{q}m}^\sigma | \Sigma^\sigma(\omega) | \varphi_{\mathbf{q}m}^\sigma \rangle$  of the self-energy

$$\Sigma_{\mathbf{q}m}^\sigma(\omega) = -\frac{i}{2\pi} \int d^3r_1 d^3r_2 d^3r_3 d^3r_4 \varphi_{\mathbf{q}m}^{\sigma*}(\mathbf{r}_1) \varphi_{\mathbf{q}m}^\sigma(\mathbf{r}_3) \times \int_{-\infty}^{\infty} T^{\sigma\sigma'}(\mathbf{r}_1, \mathbf{r}_2; \mathbf{r}_3, \mathbf{r}_4; \omega') G^{\sigma'}(\mathbf{r}_2, \mathbf{r}_4; \omega - \omega') d\omega' \quad (7)$$

with the momentum  $\mathbf{q}$ , the band index *m*, and the spin  $\sigma$  of the Bloch state  $\varphi_{\mathbf{q}m}^\sigma(\mathbf{r})$ . The short-range behavior of the screened interaction *W* in metals allows an on-site approximation to be employed [41–44]: The electron and hole are assumed to occupy the same lattice site when they interact with each other. To realize a lattice-site resolution, we formulate the theory with the help of Wannier functions

$$w_{\mathbf{R}n}^\sigma(\mathbf{r}) = \frac{1}{N} \sum_{\mathbf{k}} e^{-i\mathbf{k}\mathbf{R}} \sum_m U_{\mathbf{k}m,n}^\sigma \varphi_{\mathbf{k}m}^\sigma(\mathbf{r}), \quad (8)$$

where  $\mathbf{R}$  is the lattice site, *n* is an orbital index, and *N* is the number of  $\mathbf{k}$  points. The complex expansion coefficients  $U_{\mathbf{k}m,n}^\sigma$  of the *n*th Wannier orbital are given by projection of the eigenstates onto a muffin-tin basis function with suitable orbital character and a subsequent Löwdin orthonormalization [49]. The Wannier representation of the *T* matrix reads

$$T^{\sigma\sigma'}(\mathbf{r}_1, \mathbf{r}_2; \mathbf{r}_3, \mathbf{r}_4; \omega) = \sum_{\mathbf{R}, \mathbf{R}'} w_{\mathbf{R}n_1}^\sigma(\mathbf{r}_1) w_{\mathbf{R}'n_2}^{\sigma'*}(\mathbf{r}_2) \times T_{\mathbf{R}n_1 \mathbf{R}'n_2, \mathbf{R}'n_3 \mathbf{R}n_4}^{\sigma\sigma'}(\omega) w_{\mathbf{R}'n_3}^{\sigma*}(\mathbf{r}_3) w_{\mathbf{R}n_4}^{\sigma'}(\mathbf{r}_4). \quad (9)$$

Due to the lattice periodicity, the coefficients  $T_{\mathbf{R}n_1 \mathbf{R}'n_2, \mathbf{R}'n_3 \mathbf{R}n_4}^{\sigma\sigma'}(\omega)$  depend only on the difference vector  $\Delta\mathbf{R} = \mathbf{R} - \mathbf{R}'$ . A lattice Fourier transformation then yields

$$T_{n_1 n_2, n_3 n_4}^{\sigma\sigma'}(\mathbf{k}, \omega) = \sum_{\Delta\mathbf{R}} T_{n_1 n_2, n_3 n_4; \Delta\mathbf{R}}^{\sigma\sigma'}(\omega) e^{-i\mathbf{q}\Delta\mathbf{R}}. \quad (10)$$

Employing the Lehmann representation of the Green function

$$G^\sigma(\mathbf{r}, \mathbf{r}'; \omega) = \frac{1}{N} \sum_{\mathbf{k}} \sum_m \frac{\varphi_{\mathbf{k}m}^\sigma(\mathbf{r}) \varphi_{\mathbf{k}m}^{\sigma*}(\mathbf{r}')}{\omega - \epsilon_{\mathbf{k}m}^\sigma + i\eta \text{sgn}(\epsilon_{\mathbf{k}m}^\sigma - \epsilon_F)} \quad (11)$$

with the energies  $\epsilon_{\mathbf{k}m}^\sigma$  of the corresponding Bloch states, the Fermi energy  $\epsilon_F$ , and a positive infinitesimal  $\eta$ , one obtains for the diagonal element of the *GT* self-energy

$$\Sigma_{\mathbf{q}m}^\sigma(\omega) = -\frac{i}{2\pi} \int_{-\infty}^{\infty} d\omega' \sum_{\mathbf{k}} \sum_{n_1, n_2, n_3, n_4} T_{n_1 n_2, n_3 n_4}^{\sigma\sigma'}(\mathbf{k}, \omega') \times \sum_{m'} \frac{U_{\mathbf{q}m, n_1}^\sigma U_{\mathbf{q}-\mathbf{k}m', n_2}^{\sigma'*} U_{\mathbf{q}m, n_3}^{\sigma*} U_{\mathbf{q}-\mathbf{k}m', n_4}^{\sigma'}}{\omega - \omega' - \epsilon_{\mathbf{q}-\mathbf{k}m'}^{\sigma'} + i\eta \text{sgn}(\epsilon_{\mathbf{q}-\mathbf{k}m'}^{\sigma'} - \epsilon_F)} \quad (12)$$

where the summation over  $m'$ , in principle, runs over the infinitely many single-particle eigenstates, but in the present case the summation is effectively restricted to the ones which have been used for the construction of the Wannier basis.

The *T* matrix exhibits poles at the spin excitation energies along the real-frequency axis. The collective spin-wave excitations produce particularly strong poles at low energies, which complicates a straightforward frequency integration. The integration along the real-frequency axis can be avoided by employing the method of analytic continuation [50, 51], which is one of the two methods implemented. To this end, Eq. (12) is analytically continued to the imaginary axis and evaluated there for a set of imaginary frequencies forming a mesh along this axis. This is achieved by replacing  $\omega \rightarrow i\omega$  and  $\omega' \rightarrow i\omega'$ , formally changing the prefactor  $-i/(2\pi)$  to  $1/(2\pi)$ . In this way, one avoids the real-frequency axis where the quantities show strong variations. Along the imaginary axis, the functions are much smoother, which enables an accurate sampling and interpolation of the functions with relatively coarse frequency meshes, also simplifying the frequency convolution of Eq. (12). At the end of the calculation, the self-energy has to be analytically continued back to the real-frequency axis. We employ Padé approximants for the *T* matrix (Thiele's reciprocal difference method [52]), which allows an analytic frequency convolution with *G*, and also for the self-energy, yielding the self-energy on the whole complex frequency plane. In this approach, the self-energy is effectively represented by a sum over poles with analytically determined complex positions and weights. However, it is well known that this extrapolation can lead to spurious features in the self-energy if one of the effective poles happens to lie close to the real frequency axis.

Therefore, we have also implemented the contour deformation technique to evaluate the self-energy. This method is more accurate than analytic continuation but also requires more computation time. Details of both implementations will be presented elsewhere [53] together with a new tetrahedron method, with which the two methods yield nearly identical results. There, we also discuss a third method that could be described as a hybrid

of the two. The contour deformation technique evaluates the frequency integral of Eq. (12) explicitly, yielding the self-energy directly for real frequencies. The integration path, however, does not run along the real frequency axis from  $-\infty$  to  $\infty$  but along a deformed integration contour: from  $-\infty$  to  $i\infty$  and, at halfway, taking a *rectangular detour* at  $\omega = 0$  to capture all residues of the Green function. (The integrations from  $-\infty$  to  $-\infty$  and from  $i\infty$  to  $\infty$  do not contribute.) The resulting self-energy can be written as a sum of two terms

$$\begin{aligned} & \langle \varphi_{\mathbf{q}m}^\sigma | \Sigma^\sigma(\omega) | \varphi_{\mathbf{q}m}^\sigma \rangle \\ &= \frac{1}{N} \sum_{\mathbf{k}} \left[ \sum_{m'} \frac{1}{2\pi} \int_{-\infty}^{\infty} d\omega' \frac{T_{\mathbf{q}mm'}^{\sigma\sigma'}(\mathbf{k}, -i\omega')}{\omega + i\omega' - \epsilon_{\mathbf{q}-\mathbf{k}m'}^{\sigma'}} \right. \\ &+ \left. \begin{cases} \sum_{m'} T_{\mathbf{q}mm'}^{\sigma\sigma'}(\mathbf{k}, \omega - \epsilon_{\mathbf{q}-\mathbf{k}m'}^{\sigma'}) & \text{for } \omega < \epsilon_F \\ - \sum_{m'} T_{\mathbf{q}mm'}^{\sigma\sigma'}(\mathbf{k}, \omega - \epsilon_{\mathbf{q}-\mathbf{k}m'}^{\sigma'}) & \text{for } \omega > \epsilon_F \end{cases} \right], \end{aligned} \quad (13)$$

where  $T_{\mathbf{q}mm'}^{\sigma\sigma'}(\mathbf{k}, \omega)$  denotes the sum of the products  $TUUU$  over  $n_1, n_2, n_3$ , and  $n_4$ . The  $\mathbf{k}$  summation should be understood as a  $\mathbf{k}$  integration. It is important to perform this integration accurately. We have devised a new tetrahedron method for this purpose [53]. All results presented in this paper have been calculated with the contour deformation technique using Eq. (13).

The evaluation of Eq. (13) can be expensive. Therefore, we exploit a few symmetries to accelerate the computation. The first is a symmetry in frequency space which the  $T$  matrix inherits from the propagator  $K$  [42],  $T_{n_1 n_2, n_3 n_4}^{\sigma\sigma'}(\mathbf{k}, -i\omega) = T_{n_3 n_4, n_1 n_2}^{\sigma\sigma'*}(\mathbf{k}, i\omega)$ . This leads to  $T_{\mathbf{q}mm'}^{\sigma\sigma'}(\mathbf{k}, -i\omega) = T_{\mathbf{q}mm'}^{\sigma\sigma'*}(\mathbf{k}, i\omega)$ . Hence, we can restrict the frequency mesh to the positive imaginary axis and utilize this symmetry for the frequency integration from  $-\infty$  to  $i\infty$ . Furthermore, it follows from this symmetry that the first term of Eq. (13) is real-valued. The second term is complex in general, which will become important in Sec. V. We also exploit spatial symmetry in the evaluation of the  $\mathbf{k}$  summations. Equation (12) contains a sum over all  $\mathbf{k}$  vectors. We restrict this summation to the extended irreducible Brillouin zone (corresponding to the irreducible zone that is created by the subset of symmetry operations that leave the  $\mathbf{q}$  vector invariant [27], the so-called little group). The contribution of the symmetry-equivalent  $\mathbf{k}$  points is obtained by a symmetrization procedure employing the symmetry transformation matrices of the Wannier set [42]. In the same way, we can accelerate the computation of the two-particle propagator [Eq. (3)], which involves a  $\mathbf{k}$  summation, as well [42].

As already mentioned above, we presently refrain from combining Eq. (1) with the fully dynamical  $GW$  self-energy. Such a study is deferred to a later work. Instead, we combine it with the LSDA solution whose exchange splitting has been corrected in such a way that

the Goldstone condition (the spin-wave energy must vanish in the limit  $\mathbf{k} \rightarrow 0$ ) is fulfilled. To be more precise, we introduce a parameter  $\Delta_x$ , with which the spin-up and spin-down states are shifted with respect to each other, i.e.,  $\epsilon_{\mathbf{k}m}^{\uparrow/\downarrow} \rightarrow \epsilon_{\mathbf{k}m}^{\uparrow/\downarrow} \pm \Delta_x/2$ . (A positive  $\Delta_x$  decreases the exchange splitting.) The parameter  $\Delta_x$  is varied until the spin-wave excitation energy vanishes in the long-wavelength limit. The so-corrected single-particle system has been shown [44] to be similar to a self-consistent solution obtained with the COHSEX self-energy [36], the static limit of  $GW$ . The corrected LSDA Green function can thus be understood as an approximation to the COHSEX Green function, which is then further renormalized with the  $GT$  self-energy.

We introduce another parameter to achieve partial self-consistency in the Green function. The application of the  $GT$  self-energy does not only introduce lifetime broadening effects but also leads to an energetic shift of the electronic bands. In general, this entails that the Fermi energy has to be readjusted to ensure particle number conservation. Such a readjustment, however, has some undesired consequences. First, the spectral function vanishes at the old Fermi energy but not at the new one. Second and more seriously, spectral features, e.g., kinks in the quasiparticle bands, might end up at a wrong binding energy, in particular, if their energetic position is of the same order of magnitude as the shift of the Fermi energy. In an extreme case, the binding energy might even change sign. Clearly, in a fully self-consistent  $GT$  calculation, the Fermi energy would converge eventually, and these problems would be solved. However, presently we cannot afford such a calculation. Therefore, we employ a correction that was originally proposed by Hedin [36] and discussed in detail in Refs. 54 and 55. In a one-shot calculation, there is a mismatch between the chemical potential of the non-interacting system, inherited by the self-energy, and the chemical potential of the renormalized Green function. In order to align the two potentials, one introduces an energy shift  $\Delta_v$  in  $\Sigma(\omega) \rightarrow \Sigma(\omega - \Delta_v)$ , where  $\Delta_v$  is chosen in such a way that the Fermi energy remains unchanged by the self-energy renormalization, giving the spectral function as

$$S^\sigma(\mathbf{k}, \omega) = \frac{\text{sgn}(\epsilon_F - \omega)}{\pi} \sum_m \text{Im} \{ \omega - \epsilon_{\mathbf{k}m}^\sigma - \Sigma_{\mathbf{k}m}^\sigma(\omega - \Delta_v) \}^{-1}. \quad (14)$$

Since the corrected energies approximate COHSEX quasiparticle energies and COHSEX does not share any diagrams with  $GT$ , no subtraction of the expectation value of the exchange-correlation potential as in one-shot  $GW$  calculations is needed in this case. The spectral function in Eq. (14) is defined as the trace over the imaginary part of the renormalized Green function, the solution of the Dyson equation with the  $GT$  self-energy. The sign is chosen such that the spectral function is non-negative for all  $\omega$  and  $\mathbf{k}$  (see Sec. V).

The correction is tantamount to shifting the exchange-correlation potential by the same amount  $v_{xc}^\sigma \rightarrow v_{xc}^\sigma + \Delta_v$ .

In this way, the non-interacting reference system already contains information about the renormalized system through the shift  $\Delta_v$ , which can be regarded as some level of self-consistency. (Since the Fermi energy depends on the quasiparticle energies in the whole irreducible wedge of the Brillouin zone, the shift has to be calculated self-consistently until the Fermi energy and  $\Delta_v$  converge.) This approach solves the aforementioned two problems in a natural way.

The modification of  $v_{xc}^\sigma$  changes the single-particle energies accordingly so that, in summary, the latter are adjusted by  $\epsilon_{\mathbf{k}m}^{\uparrow/\downarrow} \rightarrow \epsilon_{\mathbf{k}m}^{\uparrow/\downarrow} + \Delta_v \pm \Delta_x/2$ , which shifts the self-energy argument in the opposite direction, effectively undoing the shift from before,  $\Sigma(\omega - \Delta_v) \rightarrow \Sigma(\omega)$ . The  $\Delta_v$  correction does not affect the Goldstone condition, which has been used to fix  $\Delta_x$ , since only the differences of the single-particle states (of opposite spins) enter the evaluation of the spin excitations energies, and not their absolute values. We note that the two parameters,  $\Delta_x$  and  $\Delta_v$ , are determined from exact physical constraints, so they do not imply a deviation from the “ab initio-ness” of the method.

With the aligned chemical potential, Eq. (14) can alternatively be written as

$$S^\sigma(\mathbf{k}, \omega) = \frac{\text{sgn}(\epsilon_F - \omega)}{\pi} \sum_m \text{Im}\{\omega - \epsilon_{\mathbf{k}m}^\sigma - \Sigma_{\mathbf{k}m}^\sigma(\omega) + \Delta_v\}^{-1}, \quad (15)$$

where the single-particle energies  $\epsilon_{\mathbf{k}m}^\sigma$  are assumed to contain the two parameters  $\Delta_x$  and  $\Delta_v$  as described above. (We note that the parameter  $\Delta_v$  in Eq. (15) seems to have no effect because the term  $-\Delta_v$  de facto cancels the  $\Delta_v$  in  $\epsilon_{\mathbf{k}m}^\sigma$ , but it should be remembered that  $\Delta_v$  shifts the Fermi energy, too. We also note that it might be surprising that a spin-independent shift of the exchange-correlation potential and, thus, of the Kohn-Sham eigenvalues should have an effect at all, but one has to remember that quasiparticle energies correspond to total-energy differences and are therefore defined absolutely.)

## V. VIOLATION OF CAUSALITY

In this section, we present a detailed discussion about the violation of causality mentioned in the introduction. To this end, we have to resort to a general second-quantization formulation of the Green function and related response quantities. The Bloch  $\mathbf{k}$  crystal momentum is suppressed for simplicity. The time-ordered Green function

$$G^\sigma(12) = -i\langle\Psi_0|\mathcal{T}[\hat{\psi}^\sigma(1)\hat{\psi}^{\sigma\dagger}(2)]|\Psi_0\rangle \quad (16)$$

comprises both the electron and the hole propagator by virtue of the time-ordering operator  $\mathcal{T}$ : If  $t_1 > t_2$ , the Heisenberg creation operator  $\hat{\psi}^{\sigma\dagger}(2)$  acts first on the many-body ground state  $|\Psi_0\rangle$  creating an electron at 2,

which is later annihilated at 1. If otherwise  $t_1 < t_2$ , then the operator  $\mathcal{T}$  switches the order of the field operators and lets  $\hat{\psi}^\sigma(1)$  act first, thus creating a hole at 1, which is later filled by an electron at 2. So, the Green function describes the propagation of an electron or a hole depending on the time order of the arguments  $t_1$  and  $t_2$ . The Fourier transformation of Eq. (16) ( $t_1 - t_2 \rightarrow \omega$ ) yields the Lehmann representation [64]

$$G^\sigma(\mathbf{r}_1, \mathbf{r}_2; \omega) = \sum_m \frac{\langle\Psi_0|\hat{\psi}_S^\sigma(\mathbf{r}_1)|\Psi_m^{\sigma+}\rangle\langle\Psi_m^{\sigma+}|\hat{\psi}_S^{\sigma\dagger}(\mathbf{r}_2)|\Psi_0\rangle}{\omega - (E_m^{\sigma+} - E_0) + i\eta} + \sum_m \frac{\langle\Psi_m^{\sigma-}|\hat{\psi}_S^\sigma(\mathbf{r}_1)|\Psi_0\rangle\langle\Psi_0|\hat{\psi}_S^{\sigma\dagger}(\mathbf{r}_2)|\Psi_m^{\sigma-}\rangle}{\omega - (E_0 - E_m^{\sigma-}) - i\eta} \quad (17)$$

where  $\eta$  is a positive infinitesimal and  $\{|\Psi_m^{\sigma\pm}\rangle, E_m^{\sigma\pm}\}$  is a complete set of energy eigensolutions of the many-body system with one spin- $\sigma$  electron more (+) or less (−) than  $|\Psi_0\rangle$ .

We now consider a diagonal element  $G_m^\sigma(\omega) := \langle\varphi_m^\sigma|G^\sigma(\omega)|\varphi_m^\sigma\rangle$  with  $\varphi_m^\sigma(\mathbf{r})$  an eigenstate of the non-interacting reference system. Since the Schrödinger field operators  $\hat{\psi}_S^\sigma(\mathbf{r})$  and  $\hat{\psi}_S^{\sigma\dagger}(\mathbf{r})$  are adjoints of each other, the numerators, when projected onto  $\varphi_m^\sigma(\mathbf{r})$ , are real and non-negative. Furthermore,  $E_0 - E_m^{\sigma-} \leq \mu \leq E_m^{\sigma+} - E_0$  with the chemical potential  $\mu$ . Then, it follows from  $(\omega \pm i\eta)^{-1} = \mathcal{P}(1/\omega) \mp i\pi\delta(\omega)$  that the imaginary part of  $G_m^\sigma(\omega)$  must have a positive (negative) sign for  $\omega < \mu$  ( $\omega > \mu$ ). As  $\eta$  enters Eq. (17) as a consequence of the time-ordering operator, we can trace the condition on the sign of  $\text{Im}G_m^\sigma(\omega)$  back to the correct time order of the field operators and thus to the causality.

The mathematical formulas derived above bear similarity with those encountered in the treatment of the *damped driven harmonic oscillator*. In this context, the energy differences would correspond to the resonance frequency of the free oscillator and  $\eta$  could be interpreted as a damping coefficient. The latter appears linearly in the imaginary part of the free oscillator’s frequency. So, a wrong sign in the imaginary part presupposes a wrong sign in  $\eta$ , which would thus have the effect of amplifying the oscillation rather than damping it. This solution could be described as one that goes backwards in time, thus violating causality.

Through the Dyson equation, the imaginary part of  $G_m^\sigma(\omega)$  can be related to the imaginary part of the self-energy

$$\text{Im}G_m^\sigma(\omega) = \frac{\text{Im}\Sigma_m^\sigma(\omega)}{[\omega - \epsilon_m^\sigma - \text{Re}\Sigma_m^\sigma(\omega)]^2 + [\text{Im}\Sigma_m^\sigma(\omega)]^2}, \quad (18)$$

where it has been used that Eq. (17) is trivially valid for the non-interacting  $G$ , too, in which case  $E_m^{\sigma+} - E_0$  and  $E_0 - E_m^{\sigma-}$  correspond to the single-particle energies  $\epsilon_m^\sigma$  and the numerators are just products of single-particle wave functions  $\varphi_m^\sigma(\mathbf{r}_1)\varphi_m^{\sigma*}(\mathbf{r}_2)$ . Equation (11) shows such a Lehmann representation formulated with Bloch vectors. We have neglected the offdiagonal elements of  $\Sigma^\sigma(\omega)$  for simplicity. According to Eq. (18),



the sign rule for  $\text{Im}G_m^\sigma(\omega)$  applies equally to  $\text{Im}\Sigma_m^\sigma(\omega)$ , also see Eq. (9.34) of [56]. In the last section, it was shown [Eq. (13)] that the imaginary part of  $\Sigma_m^\sigma(\omega)$  is completely determined by (a  $\mathbf{k}$  integration of) the imaginary part of  $T$ -matrix elements, represented in terms of single-particle eigenfunctions. From Eq. (13), it follows that the condition on the sign of  $\Sigma_m^\sigma(\omega)$  formulated above requires the imaginary part of the  $T$  matrix elements to be non-negative for all  $\omega$ .

The  $T$  matrix, as we defined it above, contains all ladder diagrams starting from third order. In this sense, we can express it as

$$T^{\sigma\sigma'} = T_{\geq 2}^{\sigma\sigma'} - T_2^{\sigma\sigma'}, \quad (19)$$

where  $T_2$  is the bare second-order ladder diagram and  $T_{\geq 2}$  includes all ladder diagrams starting from second order. This reformulation looks trivial (and it is), but it will help us to understand the reason for the violation of causality. As a first step, we realize that all ladder diagrams are flanked from either side by an interaction line  $W$ , which can be factored out giving

$$T^{\sigma\sigma'}(12, 34) = W(12)[R^{(4)\sigma\sigma'}(12, 34) - K^{\sigma\sigma'}(12, 34)]W(34). \quad (20)$$

Here,  $K$  is the free electron-hole propagator of Eq. (3) and  $R^{(4)}$  the interacting electron-hole propagator, which is related to the generalized four-point response function by  $R = -2R^{(4)}$ . Both quantities can be expressed in terms of a spin-spin correlation function [43]  $i\langle\Psi_0|\mathcal{T}[\hat{\psi}^{\sigma\dagger}(2)\hat{\psi}^{\sigma'}(1)\hat{\psi}^{\sigma\dagger}(3)\hat{\psi}^\sigma(4)]|\Psi_0\rangle$ . (Note the assumption  $\sigma' = -\sigma$ .) For the free (interacting) propagator  $K$  ( $R^{(4)}$ ), one would take  $|\Psi_0\rangle$  to be the energy ground state of the non-interacting reference (real interacting) system. The spin-spin correlation function has a similar form as Eq. (16) and can be Fourier-transformed analogously giving

$$\begin{aligned} R^{(4)\sigma\sigma'}(\mathbf{r}_1, \mathbf{r}_2, \mathbf{r}_3, \mathbf{r}_4; \omega) \\ = \sum_m \frac{\langle\Psi_m|\hat{\psi}_S^{\sigma\dagger}(\mathbf{r}_2)\hat{\psi}_S^{\sigma'}(\mathbf{r}_1)|\Psi_0\rangle\langle\Psi_0|\hat{\psi}_S^{\sigma\dagger}(\mathbf{r}_3)\hat{\psi}_S^\sigma(\mathbf{r}_4)|\Psi_m\rangle}{\omega - (E_0 - E_m) - i\eta} \\ - \sum_m \frac{\langle\Psi_0|\hat{\psi}_S^{\sigma\dagger}(\mathbf{r}_2)\hat{\psi}_S^{\sigma'}(\mathbf{r}_1)|\Psi_m\rangle\langle\Psi_m|\hat{\psi}_S^{\sigma\dagger}(\mathbf{r}_3)\hat{\psi}_S^\sigma(\mathbf{r}_4)|\Psi_0\rangle}{\omega - (E_m - E_0) + i\eta}, \end{aligned} \quad (21)$$

where  $\{|\Psi_m\rangle, E_m\}$  is a complete set of energy eigensolutions of the many-body system (with the same number of electrons as  $|\Psi_0\rangle$ ).

Inserting this expression and the corresponding one for  $K$  (which could be simplified again using the single-particle eigenstates, which is, however, not necessary for the present discussion) into Eq. (20) yields the spectral representations of the two contributions  $T_{\geq 2}$  and  $T_2$ . The  $T$  matrix elements relevant for the self-energy are obtained by multiplying with two wave-function products,  $\varphi_{m'}^{\sigma*}(\mathbf{r}_2)\varphi_{m'}^{\sigma'}(\mathbf{r}_4)$  and  $\varphi_m^{\sigma*}(\mathbf{r}_1)\varphi_m^\sigma(\mathbf{r}_3)$ , and integrating over all space coordinates. The first product originates from the Green function in Eq. (1) and the second from evaluating the diagonal element of the self-energy  $\Sigma_m^\sigma(\omega)$ , also

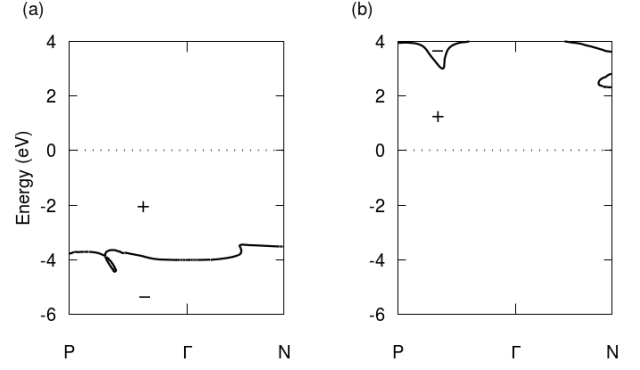


Figure 4: Map of regions where the spectral function  $S^\sigma(\mathbf{k}, \omega)$  [(a)  $\sigma = \uparrow$ , (b)  $\sigma = \downarrow$ ] of iron has positive (+) and negative (-) sign. The appearance of the negative sign implies a violation of causality, see text. The energy zero is set at the Fermi energy.

see Eq. (7). In analogy to the case of the Green function, this leads to numerators in the two terms  $T_{\geq 2}$  and  $T_2$  that are all real and non-negative. It is then straightforward to deduce from Eq. (21) that the imaginary parts of both  $T_{\geq 2}$  and  $T_2$  are non-negative in the whole frequency range. According to Eq. (13), the imaginary part of the self-energy contributions originating from  $T_{\geq 2}$  and  $T_2$  will both have the correct sign for  $\omega > \mu$  and  $\omega < \mu$  as a consequence.

Here, the decisive point is that they have the correct sign *individually*, but their difference [Eq. (20)], might have a wrong sign in some frequency region and thus violate causality. This is not just a theoretical possibility but rather an expected behavior due to a redistribution of spectral weight in the renormalized pair propagator  $R^{(4)}$  with respect to  $K$ , the free pair propagator. The imaginary part of the latter is formed by the spin-flip Stoner excitations, whereas the Bethe-Salpeter renormalization gives rise to the formation of collective excitations (spin waves) in  $R^{(4)}$  at low energies. Spectral weight thus flows from higher to lower energies so that the difference  $\text{Im}(T_{\geq 2} - T_2)$  is expected to become negative at some energy. We indeed observe this violation of causality in our calculations but have chosen to accept it, as the sign change occurs at an energy of several eV, where the lifetime broadening has already become quite small and where diagrams neglected in the present work should become more relevant and recover the correct sign.

Figure 4 shows a map of the sign of the spectral function  $S^\sigma(\mathbf{k}, \omega)$  as defined in Eq. (15) for the two spin channels in the case of iron. The causality condition demands the spectral function to be non-negative everywhere, but we do see several regions where the sign is, in fact, negative. One notices a spin asymmetry: the wrong sign appears at negative energies in the spin-up channel, whereas it is seen at positive energies in the spin-down channel. As will be explained in the next section, this spin selec-

tivity is due to the fact that a coupling to spin waves is possible only for majority holes (occupied states) and minority electrons (unoccupied states), which confirms our explanation that the causality violation originates from a shift of spectral weight from single-particle Stoner excitations to the low-energy spin waves, leading to the appearance of the wrong sign in the difference  $\text{Im}(T_{\geq 2} - T_2)$ . Both terms individually have the correct sign. In fact, if we perform the calculation with  $T_{\geq 2}$  alone (instead of the difference), the sign of the spectral function never becomes negative. However, such a calculation exhibits extreme and unphysical renormalization effects.

The lifetime broadenings in the regions with negative sign must be considered incorrect. These regions are, however, relatively far away from the Fermi energy, below  $-3.5$  eV and above  $2.5$  eV for spin up and down, respectively, and the renormalizations and lifetime broadenings close to the Fermi energy, where the  $GT$  self-energy diagrams dominate, should show the correct behavior. Clearly, if all infinitely many diagrams were included in the self-energy, the causality condition should be fulfilled. In this sense, the violation of causality is an effect of missing self-energy diagrams. For example, for larger absolute energies it is expected that the imaginary part of the  $GW$  diagram, neglected in the present work, becomes more important. In fact, there is convincing argument that already the  $GW$  self-energy term that is second order in  $v$  restores the correct sign: This term is formally similar to the self-energy contribution derived from  $T_2$  and  $K$  [Eq. (20)], except that the multiplication from both sides is with  $v$  instead of  $W$ . Since  $v(\mathbf{r}, \mathbf{r}') > W(\mathbf{r}, \mathbf{r}'; \omega = 0)$  for (nearly) all  $\mathbf{r}$  and  $\mathbf{r}'$ , it seems natural to expect the corresponding self-energy contribution (also its imaginary part) to be larger than the one from  $T_2$ . The combination of  $GT$  and  $GW$  is planned as a future study. The question of whether  $GW$  fully restores the correct sign must therefore await clarification until then.

## VI. CALCULATIONS

Figure 5 shows the  $\mathbf{k}$ - and energy-resolved spectral functions [Eq. (15)] in light blue to green together with the LSDA band structure as red lines for bcc Fe, fcc Co, and fcc Ni. The LSDA band structure is the uncorrected one (i.e.,  $\Delta_{\mathbf{x}} = \Delta_v = 0$ ), while the non-interacting reference system for the  $GT$  renormalization is taken from an LSDA solution with a parameter  $\Delta_{\mathbf{x}}$  to enforce the Goldstone condition ( $\Delta_{\mathbf{x}} = 0.10$  eV,  $0.36$  eV, and  $0.17$  eV for the three materials, respectively) and a parameter  $\Delta_v$  to align the chemical potentials of the non-interacting and interacting systems ( $\Delta_v = 190$  meV,  $76$  meV, and  $25$  meV). The parameters are discussed in Sec. IV. We employ a Wannier set of  $s$ ,  $p$ , and  $d$  orbital character constructed from the 18 lowest eigenstates in each spin channel. The Brillouin zone has been sampled with a  $14 \times 14 \times 14$   $\mathbf{k}$ -point set. The  $\mathbf{k}$  integrations of Eq. (13) are

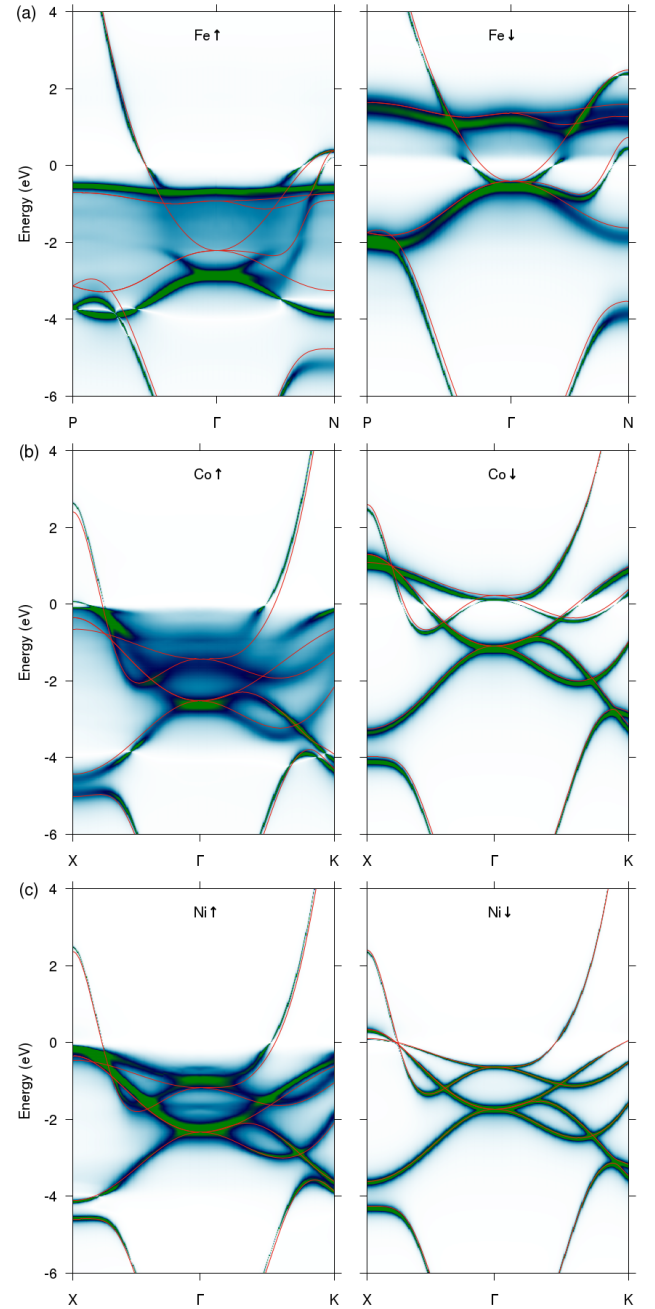


Figure 5: (Color online) Band structures of (a) Fe, (b) Co, and (c) Ni. The spectral functions [Eq. (15)] are shown in light blue to green. The LSDA band structure is shown as red lines for comparison. The energy zero is set at the Fermi energy. The lifetime broadening decreases in the order of increasing  $d$  occupancy (Fe $\rightarrow$ Co $\rightarrow$ Ni). The spin and particle-hole asymmetries in the lifetime broadening are clearly seen.

carried out using a newly developed tetrahedron method [53].

For the first term of Eq. (13), we employ a frequency mesh along the imaginary axis containing 20 points from 0 to  $2i$  htr. A Padé approximant, determined from these 20 points, yields  $T_{\mathbf{q}mm'}^{\sigma\sigma'}(\mathbf{k}, i\omega)$  for the complete imagi-

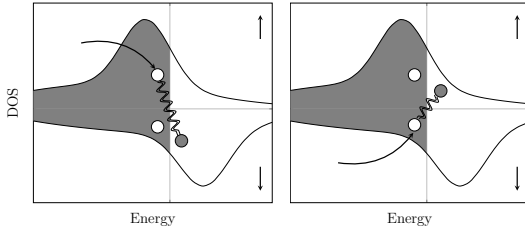


Figure 6: Schematic illustration of the scattering of majority (left) and minority holes (right) in a ferromagnet. The scattering phase space of the former is much larger than that of the latter.

nary axis (interpolating between the points and extrapolating beyond  $2i\hbar\tau$ ) and enables an analytic integration along  $i\omega$ . For the second term of Eq. (13), the matrix  $T_{\mathbf{q}mm'}^{\sigma\sigma'}(\mathbf{k}, \omega)$  is calculated for real frequencies  $\omega$  in steps of 20 meV. The self-energy  $\Sigma_{\mathbf{q}m}^{\sigma}(\omega)$  is evaluated on a mesh between  $-6$  eV and  $4$  eV (with respect to the Fermi energy) with a step size of 50 meV. To achieve very high resolution in energy, necessary to resolve sharp quasiparticle peaks (as found close to the Fermi energy), a spline interpolation is applied to obtain spectral functions in steps of 2 meV. The calculations were carried out on the supercomputer JURECA at the Jülich Supercomputing Centre [57].

Looking closely at the regions around the Fermi energy, one realizes that the lifetime broadenings disappear at energy zero and grow rapidly for lower and higher energies. Beyond a binding energy of around 4 eV (negative energies in the diagrams) in the spin-up channel, they decrease again (even to the extent that the sign changes to negative, see Sec. V.) The reason for this is the restriction of the self-energy to the  $GT$  diagram, which is expected to give the low-energy scattering contribution because of the low energies of the magnon excitations contained in the  $T$  matrix. At higher binding energies, other diagrams, which are neglected in the present study, should become increasingly important, for example, the  $GW$  diagram.

The lifetime broadening is strongest in bcc Fe and weakens in the order of  $d$  occupancy (Fe $\rightarrow$ Co $\rightarrow$ Ni). This is due to the decrease of the number of available minority conduction states, into which a majority electron can be excited, thus reducing the phase space of spin excitations. We also observe a spin asymmetry of the lifetime effects: the majority valence states are broadened more strongly than the minority ones. This can be attributed to the spin asymmetry of the density of states. The scattering diagram shown in Fig. 3 may be described as an incoming majority hole at 1, which excites an electron-hole pair at 2 in the minority channel. The majority hole and minority electron then propagate through the system, successively scattering with each other until the minority electron-hole pair recombines at 4. The correlated propagation of the electron and the hole (having opposite spins) embodies the spin-flip excitations in the

form of Stoner excitations and, due to their correlated motion, also of the collective spin-wave excitations. The probability for the pair formation and the pair propagation process depends on the number of available majority valence and minority conduction states, which is large in this case, see Fig. 6, left. (We note that the states also have similar orbital character.) On the other hand, an incoming minority hole would have to combine with majority conduction states. Naturally, the available phase space is much smaller in this case (Fig. 6, right), which explains the spin asymmetry in the lifetime broadening. The fact that minority bands are visible down to much larger binding energies than majority bands in ARPES is thus revealed to be a lifetime effect caused by electron-electron scattering. It should be noted that the qualitative behavior has already been observed in previous studies based on DMFT [18–20, 22] and model calculations [58]. Our calculated spectral functions for iron are remarkably similar to the ones published in Ref. 22. However, the fact that both the magnon excitation spectrum and the  $GT$  self-energy are fully  $\mathbf{k}$  dependent in our method gives rise to additional fine structure in the spectral functions, e.g., band anomalies, which have not been observed in theoretical studies so far.

Apart from the spin asymmetry, there is evidence for a particle-hole asymmetry as well, i.e., a markedly different lifetime broadening above and below the Fermi energy; namely, in the majority channels of all three materials and also in the minority channel of Fe. Here, an explanation very similar to the one just given would predict the lifetime broadening of majority hole (minority electron) bands to be larger than the broadening of majority electron (minority hole) bands, in agreement with the spectra.

In iron, and to a lesser degree in Co, the many-body renormalization is so strong that the quasiparticle character is virtually lost between  $-2.5$  and  $-0.5$  eV in the majority channel. A similar but less pronounced renormalization effect is also seen in the minority channel of iron at around 0.5 eV above the Fermi energy, see below. The  $GT$  self-energy thus leads to a substantially more complex spectral function than the quasiparticle band structure of a  $GW$  calculation, let alone the mean-field band structure of Kohn-Sham DFT. In the case of the former, one often only plots the energy-renormalized quasiparticle bands and drops the lifetime broadening altogether, which is legitimate because the main self-energy poles of  $GW$  are typically energetically far away from the valence and low-lying conduction bands. The quasiparticle approximation is therefore a good one. To be more precise, the main  $GW$  self-energy poles describe the coupling of the electrons and holes to plasmons (emission and absorption of plasmons), whose energies  $\approx \epsilon_P$  are typically in the order of tens of eV. The poles, thus, appear well separated from the valence (conduction) band energies  $\epsilon_{\mathbf{k}m}^{\sigma}$  at around  $\epsilon_{\mathbf{k}m}^{\sigma} \mp \epsilon_P$  for valence and conduction states, respectively. As a result, one obtains a well-defined renormalized quasiparticle band structure

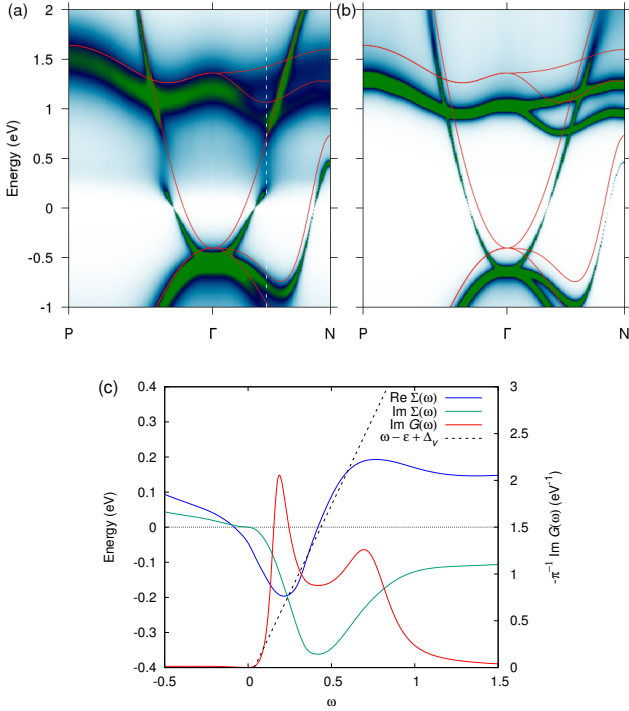


Figure 7: (Color online) (a) Closeup of dispersion anomalies in a spin-down conduction band of iron. The LSDA bands are shown in red for comparison. (b) Same band renormalized only with the lowest-order diagram, which is of third order in  $W$ , see Fig. 1, and which cannot describe the scattering of electrons and spin waves. The anomaly disappears. The anomaly in (a) can therefore be attributed to electron–spin-wave scattering. (c) Spectral function (red line) along the white dashed line marked in (a). Real and imaginary parts of the self-energy are shown as blue and green lines, respectively. The spectral-function peaks are roughly at the intersections of the blue curve with a linear function, see text.

and, at a much larger energy, the corresponding plasmon satellites. In the  $GT$  self-energy, on the other hand, the plasmon energies  $\epsilon_P$  would have to be replaced by the much smaller magnon energies  $\approx \epsilon_M$ . Furthermore, the spin of the Green function in the  $GT$  self-energy is opposite to that of the self-energy itself [see Eq. (1)]. So, the  $GT$  self-energy poles are to be expected at energies shifted from the *opposite-spin* band energies, i.e., at around  $\epsilon_{\mathbf{k}m}^{-\sigma} \mp \epsilon_M$ . In this sense, the magnon energies additionally compete with the exchange splitting. To sum up, the  $GT$  self-energy poles will fall straight into the valence (and low-lying conduction) region, giving rise to a much richer photoelectron spectrum than, for example, in  $GW$  calculations.

The plot of the  $\mathbf{k}$ - and energy-resolved spectral function allows fine details of the quasiparticle band structure to be investigated. The resonant interaction with many-body states in the valence band region (these form the pole structure of the self-energy) can give rise to anomalies in the band dispersion and satellite bands, as we will discuss exemplarily for a few cases in the following.

We first analyze a band anomaly in a spin-down conduction band of iron about 500 meV above the Fermi energy, see Fig. 5(a), right panel. A closeup is shown in Fig. 7(a). Whereas the respective Kohn-Sham band (red lines) is continuous and shows an approximately parabolic dispersion, the renormalized quasiparticle band seems to be cut in two: the band breaks off at around 250 meV and reappears at 700 meV with an incoherent continuum in-between. The energetic position of the anomaly, immediately above the Fermi energy, indicates that electronic scattering with low-energy spin waves is responsible for its formation. This is confirmed by Fig. 7(b), which shows the band structure renormalized with only the first term of Eq. (2). This term, the third-order diagram of Fig. 3, can be regarded as not containing scattering contributions with collective spin-wave excitations, which, in turn, would require an infinite (or at least large) number of ladder diagrams to be summed to become a well defined many-body excitation. Fig. 7(b) does not exhibit any band anomaly in the respective bands [65]. This proves that the scattering with spin waves is responsible for the appearance of the band anomaly. It also explains why DMFT cannot reproduce the anomaly because DMFT spatially confines the bosonic excitations in the impurity, which prevents the spin waves to become well-defined extended many-body excitations, despite the fact that infinitely many ladder diagrams are summed in principle. The spatial confinement in DMFT is equivalent to the missing  $\mathbf{k}$  dependence of the bosonic excitation spectrum. In contrast, this  $\mathbf{k}$  dependence (and also the one for the self-energy) is fully preserved in our theoretical approach.

The electron-magnon interaction gives rise to a double-peak structure in the spectral function at the Bloch momentum of the anomaly [white dashed line in Fig. 7(a)]. Figure 7(c) shows this spectral function as the red curve. The blue and green lines show the real and imaginary components of the self-energy matrix element  $\Sigma_{\mathbf{k}m}^{\sigma}(\omega) = \langle \varphi_{\mathbf{k}m}^{\sigma} | \Sigma^{\sigma}(\omega) | \varphi_{\mathbf{k}m}^{\sigma} \rangle$ , respectively, where  $\varphi_{\mathbf{k}m}^{\sigma}$  is the respective Kohn-Sham state. The spectral function clearly exhibits two peaks. In general, peaks in the spectral function are expected where the denominator of Eq. (15) becomes small, i.e., where the linear function  $\omega - \epsilon_{\mathbf{k}m}^{\sigma} + \Delta_v$  becomes identical or, at least, close to the self-energy  $\Sigma_{\mathbf{k}m}^{\sigma}(\omega)$ . In fact, the two peaks are seen close to the intersections of the linear function (black dashed line) with the real part of the self-energy (blue line), whereas its imaginary part slightly shifts the peak positions and also suppresses a possible third peak related to the intersection in the middle. [If the self-energy is assumed to be given by a single pole  $(\omega - \omega_0)^{-1}$  with a complex self-energy resonance at  $\omega_0$ , then equating with the linear function would yield a quadratic equation with only two possible solutions.]

One might be tempted to identify one of the two peaks as the quasiparticle peak and the other as the magnon satellite, roughly corresponding to the two energies  $\epsilon_{\mathbf{k}m}^{\sigma}$  and  $\epsilon_{\mathbf{k}m}^{-\sigma} + \epsilon_M$  discussed above. However, this is not quite

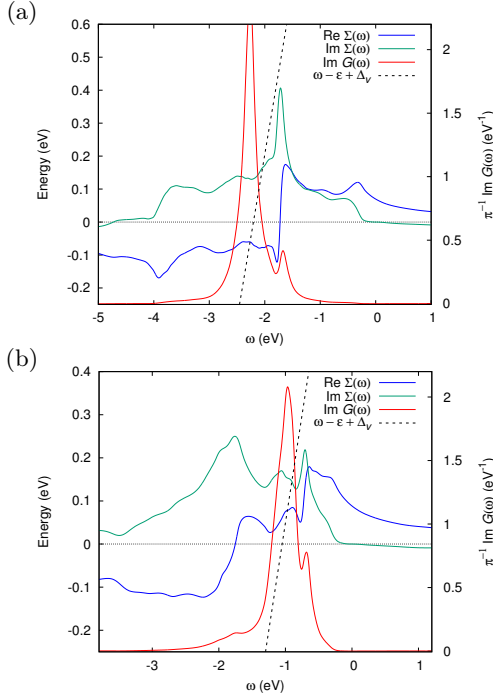


Figure 8: (Color online) Same as Fig. 7(c) for the two secondary bands [(a) upper one, (b) lower one] seen in the spin-up channel of nickel of Fig. 5(c). The spectral function and self-energy are plotted for the  $\Gamma$  point.

correct because it would disregard the coupling between these two fundamental many-body states. Let us consider a simple  $2 \times 2$  Hamiltonian with the above two energies on the diagonal. The offdiagonal (coupling) matrix elements must be nonzero, otherwise there would not be any renormalization. As the quasiparticle band  $\epsilon_{\mathbf{k}m}^{\sigma}$  disperses upwards in energy, it approaches and transverges the energy  $\epsilon_{\mathbf{k}m}^{-\sigma} + \epsilon_M$ . The coupling and the strong lifetime effects make the band disappear. When the distance between the two energies has again grown large enough, the quasiparticle band reappears. The two peaks show up when the diagonal elements are roughly identical. The peak separation can then be identified as a measure for the electron-magnon coupling strength (offdiagonal elements).

In the renormalized majority band structure of nickel, Fig. 5(c), one observes two curious *secondary* bands close to the center of the Brillouin zone, a weak one above the highest valence band and a somewhat stronger one between the highest and the second highest band. The latter one even seems to trace the dispersion of the quasiparticle bands below. Although the features look very different to the band anomaly discussed before, they have a similar origin. One might imagine the two energies  $\epsilon_{\mathbf{k}m}^{\sigma}$  and  $\epsilon_{\mathbf{k}m}^{-\sigma} - \epsilon_M$  to be nearly constant with respect to the Bloch vector  $\mathbf{k}$ . The two peaks, the strong quasiparticle and the weak secondary one, then form two nearly parallel bands with little variation in strength. Figs. 8(a) and (b) show the spectral function, together with the self-

energy and the linear function  $\omega - \epsilon_{\mathbf{k}m}^{\sigma} + \Delta_v$ , at the  $\Gamma$  point ( $k = 0$ ). In contrast to Fig. 7(c), the two spectral-function peaks are of very different strength. The small secondary peak cannot be related to an intersection of the black dashed line with the blue solid one. It rather appears where the two functions have the closest approach. Due to the very different peak strengths, one can interpret the strong peak as the quasiparticle peak and the secondary one as a magnon satellite peak (the corresponding many-body states having small admixtures of each other). It might seem a curiosity that the satellite peak appears *above* the quasiparticle peak instead below, as one is used to from *GW* calculations. This can be attributed to the exchange splitting, which, as discussed above, competes with the magnon energy and can cause the satellite peak to emerge *on the wrong side*, according to  $\epsilon_{\mathbf{k}m}^{-\sigma} + \epsilon_M = \epsilon_{\mathbf{k}m}^{\sigma} - \epsilon_M + \Delta_{\mathbf{k}m}$  with the exchange splitting  $\Delta_{\mathbf{k}m}$ .

In iron and cobalt, we clearly see the onset of strong lifetime broadening when the quasiparticle bands suddenly lose intensity, and a “waterfall” structure forms. The “waterfall” structures seen here are very similar to a feature often observed in ARPES spectroscopy. This feature is interpreted as a footprint of a many-body resonance, at whose energy the spectral function is expected to show non-Fermi liquid behavior. The interpretation is confirmed by the present calculations.

The “waterfall” structures are observed roughly at 250-600 meV in Fe [Fig. 9(a)] and at 200-500 meV in Co [Fig. 5(b)]. Nickel, on the other hand, exhibits the weakest lifetime broadening of all. While it is still strong, it does not lead to the disappearance of the quasiparticle character as in Fe and Co. The quasiparticle bands, although substantially broadened, remain well-defined over the whole energy range. Nevertheless, one can still make out a slight waterfall shape in the strongly dispersing band between  $\Gamma$  and K. In one of the bands of Fe, one can discern a slight kink in the band dispersion at about 250 meV, just where the lifetime broadening sets in. Cui *et al.* [59] published ARPES spectra of iron and claimed an anomaly in a majority band at around 270 meV to originate from electron-magnon interactions. However, in Ref. 60 they distanced themselves from this claim and attributed the anomaly to an inaccuracy of the line-shape analysis in case of strong lifetime broadening. Indeed, our theoretical spectra do not exhibit a dispersion anomaly in the band they have measured.

In the following, we investigate another band anomaly in a minority band of iron at the relatively large binding energy of 1.5 eV. Interestingly, very recently, an anomaly was found in ARPES experiments in the same minority band and roughly at the same energy and momentum as predicted by our theoretical calculation. We report about this comparison elsewhere (Ref. 15) in detail. Figure 9(b) and (c) present the theoretical (minority) spectral functions together with a comparison to the peak fits (red crosses) of the experimental momentum distribution curves. The two calculations (b) and (c) differ in the pa-



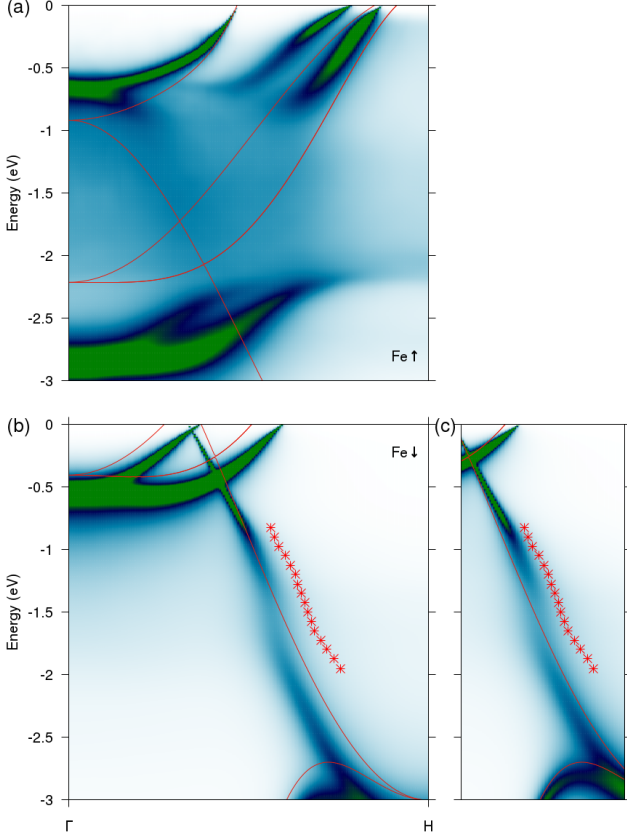


Figure 9: (Color online) Renormalized band structure of iron in the (a) majority and (b) minority channel. High-energy anomaly in a minority band of iron. (a) and (b) *GT*-renormalized spectral function with  $\Delta_v = 190$  meV and (c)  $\Delta_v = 0$ . The LSDA bands are shown as red lines. The red crosses are fitted peak positions from experiment (data reproduced from Ref. 15).

parameter  $\Delta_v = 190$  meV and  $\Delta_v = 0$ . The form of the two plots is very similar, implying that the spectral function is largely unaffected by the parameter  $\Delta_v$  at higher binding energies. In Ref. 15, we only show the spectrum for  $\Delta_v = 0$ , which is why we have included this result here for comparison.

After what we have discussed before, it might seem contradictory that a band anomaly should appear in a minority valence band. In fact, the scattering phase space is smaller for the minority valence states, but it is not zero. It does contain spin-flip Stoner excitations to which a propagating hole can couple. And, in the present case, these Stoner excitations form a particularly strong intensity in the spin excitation spectrum at around 0.7 eV [15]. The many-body resonance is then formed by the Stoner pairs (spin  $+\hbar$ ) together with majority hole *d* states (spin  $-\hbar/2$ ) that form a pronounced peak in the density of states at around 0.8 eV. This resonance is strong enough to give rise to the observed anomaly in the minority hole band (spin  $+\hbar/2$ ) at a binding energy of 1.5 eV. We note

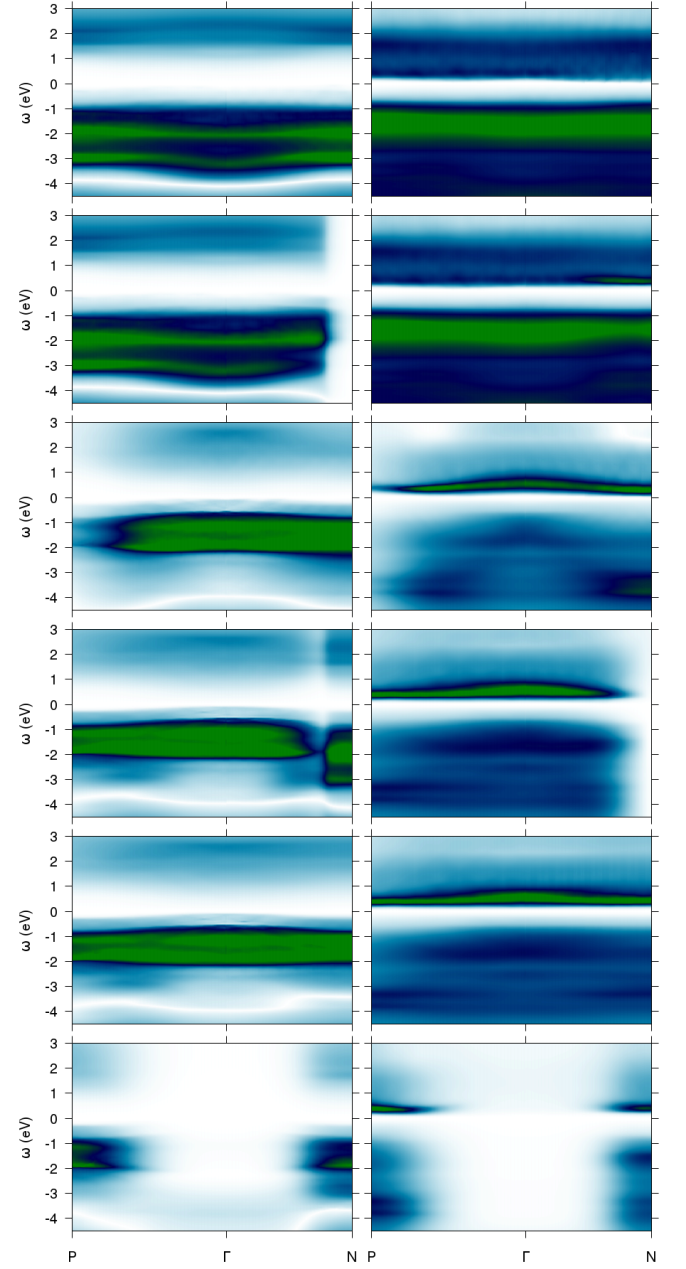


Figure 10: (Color online) Momentum and frequency dependence of the self-energy for iron. The imaginary component  $|\text{Im } \Sigma_{\mathbf{q}m}^{\sigma}(\omega)|$  is shown for the bands marked in color in Fig. 11, from bottom to top: green, blue, red, magenta, orange, black; left column spin up, right column spin down.

at this point that the shape of the band anomaly can again be described as a “waterfall” structure.

The present method fully retains the  $\mathbf{k}$  dependence of both the bosonic (magnonic) excitation spectrum and the self-energy. This is in contrast to the DMFT approach, in which the spatial confinement to the impurity effectively obliterates the  $\mathbf{k}$  dependence of the quantities. This leads to the fact that band anomalies that are caused by a coupling to extended spin waves are properly described in the

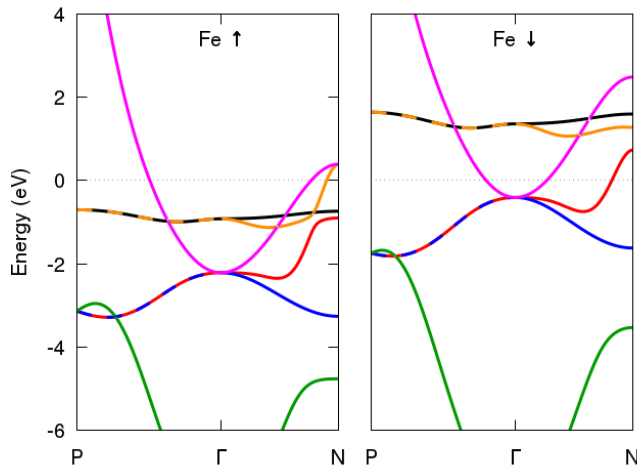


Figure 11: (Color online) Kohn-Sham LSDA band structure of iron. The colors mark the different bands for which the self-energy is plotted in Fig. 10.

present method but might be missed in DMFT, see, e.g., Fig. 7(a). The  $\mathbf{k}$  dependence of the spin excitation spectrum has been described already in Refs. [41–44] among other works. However, we also have the possibility to directly investigate the  $\mathbf{k}$  dependence of the self-energy. To this end, we have plotted the self-energy matrix elements  $\Sigma_{\mathbf{k}m}^{\sigma}(\omega)$  in Fig. 10. The respective bands are marked in color in Fig. 11. Overall, we observe a relatively weak dependence of the self-energy on the Bloch momentum, in particular for the localized  $d$  bands. However, some bands do show a strong  $\mathbf{k}$  dependence, especially the more strongly dispersing bands, such as the green band (Fig. 11). We also see the effect of hybridization: For example, the spin-up red and orange curves strongly hybridize close to the N point and exchange orbital character. This is reflected in the self-energies, which, towards the right, seem to exchange roles. Again, we would like to emphasize that a weak  $\mathbf{k}$  dependence of the self-energy does not necessarily speak in favor of a purely local treatment of correlation effects. Equally important, or arguably more important, is the  $\mathbf{k}$  dependence of the bosonic excitation spectrum. A purely local treatment would turn the quadratic spin-wave branch into an incoherent broad peak, which might wash out resonances of the electron-magnon scattering.

## VII. CONCLUSIONS

In summary, we have described a Green-function technique to calculate the electron-magnon scattering from first principles. The  $GT$  self-energy is constructed from the product of the single-particle Green function  $G$  and the multiple scattering  $T$  matrix, which can be viewed as an effective interaction that acts through the exchange of magnons. The  $T$  matrix, thus, contains the full spin

excitation spectrum, comprising collective spin-wave and single-particle Stoner excitations, and, diagrammatically, it describes the correlated motion of an electron-hole pair of opposite spins. When expanded in powers of the screened Coulomb interaction  $W$ , the  $T$  matrix can be written as a summation over ladder diagrams of ever increasing order. We have shown that a formulation consistent with the Hedin equations requires the  $GT$  self-energy to include the third-order ladder diagram as the lowest order. In this way, the self-energy approximation is free of double counting with the Hartree or exchange ( $GW$ ) diagrams.

We showed that the so-constructed  $GT$  self-energy can lead to a violation of causality, manifesting itself in an incorrect sign change of the spectral function. We elucidated the mathematical reason for this violation of causality: The particular subset of  $GT$  diagrams can be written as the difference of two terms, respectively containing the renormalized and the bare electron-hole propagator. The renormalization redistributes the spectral weights in such a way that the difference can become negative in a certain energy region. However, since the sign change occurs far away from the Fermi energy, we accept this violation of causality and show that the resulting renormalized band structures yield a correct description of the electron-magnon scattering around the Fermi energy. It is expected that other diagrams neglected in the present work, in particular, the  $GW$  self-energy, will act to restore the correct sign of the spectral function. However, this goes beyond the scope of the present study.

The  $GT$  self-energy gives rise to a very strong lifetime broadening of the quasiparticle bands, to the extent that in a certain energy region the quasiparticle character is virtually lost in the majority valence bands of bcc Fe and fcc Co. The minority bands, however, are much less affected by the lifetime broadening, which we have attributed to the spin asymmetry of the density of states. For a similar reason, one also finds a particle-hole asymmetry. The spin asymmetry in the lifetime broadening explains the experimental fact that minority bands are seen to relatively large binding energies, while the majority bands disappear very soon below the Fermi energy. The strong renormalization effects also give rise to “waterfall” structures in the  $\mathbf{k}$ - and energy-resolved spectral functions, in particular for bcc Fe and fcc Co.

The  $T$  matrix contains the acoustic spin-wave excitations for all wave vectors, including the long-wavelength limit  $\mathbf{k} \rightarrow 0$ , where the excitation energy vanishes and the  $T$  matrix becomes singular with a mathematical delta peak in its imaginary part. Since such a singularity is likely to give rise to numerical difficulties, we have investigated its contribution to the  $GT$  self-energy. As a result, the contribution of the long-wavelength spin-wave excitation should be very small in the problematic limit  $\mathbf{k} \rightarrow 0$ .

The contribution of the spin-wave excitations do not vanish for finite  $k$ , though. Our numerical calculations have shown that it is this contribution that can lead to

the formation of dispersion anomalies in majority valence and minority conduction bands. There, the spectral function can exhibit double-peak structures, which may be interpreted as a quasiparticle and a magnon satellite peak. However, when the peaks are of equal strength, they are general mixtures of the two and the peak separation can be regarded as a measure of the electron-magnon coupling strength.

Our method can describe a band-dispersion anomaly in the minority channel of bcc Fe at a large binding energy of about 1.5 eV, which has very recently been observed in ARPES measurements [15]. Whereas such a large energy is commonly not associated with a magnon excitation, we could elucidate [15] that this band anomaly is caused by a many-body resonance formed by a superposition of Stoner excitations (an increased Stoner intensity is seen in the spin excitation spectrum at around 0.7 eV) and majority hole states that form a peak in the density of states (at around 0.8 eV).

While the overall shape of the renormalized band structures is similar to corresponding DMFT calculations, the latter have not been able to describe the band anomalies discussed in the present paper. We attribute this to the main approximation of the DMFT approach, the spatial confinement of the electronic correlation to a single impurity site. This neglects the  $\mathbf{k}$  dependence of the self-energy, but, more importantly, it also does not allow for

a  $\mathbf{k}$  dependent bosonic (magnonic) excitation spectrum, effectively replacing the well-defined quadratic branch of extended spin waves by a broad feature of local excitations that cannot couple strongly to electrons.

In summary, we believe that the present work is an important step in the development of ab initio many-body methods for the treatment of magnetic materials, in which the magnon energies (collective and Stoner type), the exchange splitting, the band energies, and the electron-magnon coupling strength set different energy scales that compete with each other. Further studies in this direction might also elucidate the role of magnons in the potential formation of Cooper pairs in high-temperature superconductors.

### Acknowledgments

The authors acknowledge valuable discussions with Ewa Młyńczak, Lukas Plucinski, Ersoy Şaşıoğlu, Markus Betzinger, Manuel dos Santos Dias, Ferdi Aryasetiawan, and Hans Lustfeld. We thank Irene Aguilera for a critical reading of the manuscript. We gratefully acknowledge the computing time granted through JARA-HPC on the supercomputer JURECA at Forschungszentrum Jülich.

- 
- [1] I. Žutić, J. Fabian, and S. Das Sarma, *Rev. Mod. Phys.* **76**, 323 (2004).
  - [2] A. H. MacDonald, T. Jungwirth, and M. Kasner, *Phys. Rev. Lett.* **81**, 705 (1998).
  - [3] T. Balashov, A. F. Takács, W. Wulfhekel, and J. Kirschner, *Phys. Rev. Lett.* **97**, 187201 (2006).
  - [4] T. Balashov, A. F. Takács, M. Däne, A. Ernst, P. Bruno, and W. Wulfhekel, *Phys. Rev. B* **78**, 174404 (2008).
  - [5] B. Schweefinghaus, M. dos Santos Dias, A. T. Costa, and S. Lounis, *Phys. Rev. B* **89**, 235439 (2014).
  - [6] B. Schweefinghaus, Ph.D. thesis, RWTH Aachen (2016).
  - [7] E. Dagotto, *Rev. Mod. Phys.* **66**, 763 (1994).
  - [8] D. Scalapino, *Physics Reports* **250**, 329 (1995).
  - [9] K. Sasmal, B. Lv, B. Lorenz, A. M. Guloy, F. Chen, Y.-Y. Xue, and C.-W. Chu, *Phys. Rev. Lett.* **101**, 107007 (2008).
  - [10] T. Dahm, V. Hinkov, S. V. Borisenko, A. A. Kordyuk, V. B. Zabolotnyy, J. Fink, B. Büchner, D. J. Scalapino, W. Hanke, and B. Keimer, *Nat. Phys.* **5**, 217 (2009).
  - [11] S. Monastera, F. Manghi, C. A. Rozzi, C. Arcangeli, E. Wetli, H.-J. Neff, T. Greber, and J. Osterwalder, *Phys. Rev. Lett.* **88**, 236402 (2002).
  - [12] R. Knorren, K. H. Bennemann, R. Burgermeister, and M. Aeschlimann, *Phys. Rev. B* **61**, 9427 (2000).
  - [13] J. Schäfer, D. Schrupp, E. Rotenberg, K. Rossnagel, H. Koh, P. Blaha, and R. Claessen, *Phys. Rev. Lett.* **92**, 097205 (2004).
  - [14] A. Hofmann, X. Y. Cui, J. Schäfer, S. Meyer, P. Höpfner, C. Blumenstein, M. Paul, L. Patthey, E. Rotenberg, J. Bünenmann, et al., *Phys. Rev. Lett.* **102**, 187204 (2009).
  - [15] E. Mlyńczak, M. C. T. D. Müller, P. Gospodarcic, T. Heider, I. Aguilera, G. Bihlmayer, M. Gehlmann, M. Jugovac, G. Zamborlini, C. Tusche, et al., *Nature Communications* **10**, 505 (2019).
  - [16] A. Georges, G. Kotliar, W. Krauth, and M. J. Rozenberg, *Rev. Mod. Phys.* **68**, 13 (1996).
  - [17] G. Kotliar, S. Y. Savrasov, K. Haule, V. S. Oudovenko, O. Parcollet, and C. A. Marianetti, *Rev. Mod. Phys.* **78**, 865 (2006).
  - [18] M. I. Katsnelson and A. I. Lichtenstein, *Journal of Physics: Condensed Matter* **11**, 1037 (1999).
  - [19] A. Grechnev, I. Di Marco, M. I. Katsnelson, A. I. Lichtenstein, J. Wills, and O. Eriksson, *Phys. Rev. B* **76**, 035107 (2007).
  - [20] J. Sánchez-Barriga, J. Fink, V. Boni, I. Di Marco, J. Braun, J. Minár, A. Varykhalov, O. Rader, V. Bellini, F. Manghi, et al., *Phys. Rev. Lett.* **103**, 267203 (2009).
  - [21] J. Sánchez-Barriga, J. Minár, J. Braun, A. Varykhalov, V. Boni, I. Di Marco, O. Rader, V. Bellini, F. Manghi, H. Ebert, et al., *Phys. Rev. B* **82**, 104414 (2010).
  - [22] J. Sánchez-Barriga, J. Braun, J. Minár, I. Di Marco, A. Varykhalov, O. Rader, V. Boni, V. Bellini, F. Manghi, H. Ebert, et al., *Phys. Rev. B* **85**, 205109 (2012).
  - [23] G. Onida, L. Reining, and A. Rubio, *Rev. Mod. Phys.* **74**, 601 (2002).
  - [24] W. G. Aulbur, L. Jönsson, and J. W. Wilkins (Academic Press, Cambridge MA, 1999), vol. 54 of *Solid State Physics*, pp. 1 – 218.
  - [25] A. Yamasaki and T. Fujiwara, *Journal of the Physical Society of Japan* **72**, 607 (2003).



- [26] F. Aryasetiawan, Phys. Rev. B **46**, 13051 (1992).
- [27] C. Friedrich, S. Blügel, and A. Schindlmayr, Phys. Rev. B **81**, 125102 (2010).
- [28] D. E. Eastman, F. J. Himpsel, and J. A. Knapp, Phys. Rev. Lett. **44**, 95 (1980).
- [29] H. Höchst, S. Hüfner, and A. Goldmann, Zeitschrift für Physik B Condensed Matter **26**, 133 (1977).
- [30] F. J. Himpsel, J. A. Knapp, and D. E. Eastman, Phys. Rev. B **19**, 2919 (1979).
- [31] W. Eberhardt and E. W. Plummer, Phys. Rev. B **21**, 3245 (1980).
- [32] P. Heimann, F. Himpsel, and D. Eastman, Solid State Communications **39**, 219 (1981).
- [33] R. Kirby, E. Kisker, F. King, and E. Garwin, Solid State Communications **56**, 425 (1985).
- [34] H. Höchst, A. Goldmann, and S. Hüfner, Zeitschrift für Physik B Condensed Matter **24**, 245 (1976).
- [35] H. Höchst, S. Hüfner, and A. Goldmann, Physics Letters A **57**, 265 (1976).
- [36] L. Hedin, Phys. Rev. **139**, A796 (1965).
- [37] M. Springer, F. Aryasetiawan, and K. Karlsson, Phys. Rev. Lett. **80**, 2389 (1998).
- [38] V. P. Zhukov, E. V. Chulkov, and P. M. Echenique, Phys. Rev. Lett. **93**, 096401 (2004).
- [39] P. Romaniello, F. Bechstedt, and L. Reining, Phys. Rev. B **85**, 155131 (2012).
- [40] F. Aryasetiawan and K. Karlsson, Phys. Rev. B **60**, 7419 (1999).
- [41] E. Şaşıoğlu, A. Schindlmayr, C. Friedrich, F. Freimuth, and S. Blügel, Phys. Rev. B **81**, 054434 (2010).
- [42] C. Friedrich, E. Şaşıoğlu, M. Müller, A. Schindlmayr, and S. Blügel, in *First Principles Approaches to Spectroscopic Properties of Complex Materials*, edited by C. Di Valentin, S. Botti, and M. Cococcioni (Springer Berlin Heidelberg, 2014), vol. 347 of *Topics in Current Chemistry*, pp. 259–301.
- [43] C. Friedrich, M. C. T. D. Müller, and S. Blügel, in *Handbook of Materials Modeling. Volume 1 Methods: Theory and Modeling*, edited by S. Yip and W. Andreoni (Springer Berlin Heidelberg, 2018).
- [44] M. C. T. D. Müller, C. Friedrich, and S. Blügel, Phys. Rev. B **94**, 064433 (2016).
- [45] T. Moriya, *Spin Fluctuations in Itinerant Electron Magnetism* (Springer Berlin Heidelberg, 1985).
- [46] Y. Nambu, Phys. Rev. **117**, 648 (1960).
- [47] J. Goldstone, Il Nuovo Cimento **19**, 154 (1961).
- [48] <http://www.flapw.de>.
- [49] F. Freimuth, Y. Mokrousov, D. Wortmann, S. Heinze, and S. Blügel, Phys. Rev. B **78**, 035120 (2008).
- [50] H. N. Rojas, R. W. Godby, and R. J. Needs, Phys. Rev. Lett. **74**, 1827 (1995).
- [51] M. M. Rieger, L. Steinbeck, I. White, H. Rojas, and R. Godby, Computer Physics Communications **117**, 211 (1999).
- [52] G. Baker and P. Graves-Morris, *Padé Approximants*, Encyclopedia of Mathematics and its Applications (Cambridge University Press, Cambridge UK, 2010).
- [53] C. Friedrich (2019), submitted.
- [54] A. Schindlmayr, Phys. Rev. B **56**, 3528 (1997).
- [55] T. J. Pollehn, A. Schindlmayr, and R. W. Godby, Journal of Physics: Condensed Matter **10**, 1273 (1998).
- [56] A. L. Fetter and J. D. Walecka, *Quantum theory of many-particle systems* (McGraw-Hill, New York, 1971).
- [57] D. Krause and P. Thörnig, Journal of large-scale research facilities **4**, A132 (2019).
- [58] J. Hong and D. L. Mills, Phys. Rev. B **59**, 13840 (1999).
- [59] X. Cui, K. Shimada, M. Hoesch, Y. Sakisaka, H. Kato, Y. Aiura, M. Higashiguchi, Y. Miura, H. Namatame, and M. Taniguchi, Surface Science **601**, 4010 (2007), eCOSS-24.
- [60] X. Y. Cui, K. Shimada, Y. Sakisaka, H. Kato, M. Hoesch, T. Oguchi, Y. Aiura, H. Namatame, and M. Taniguchi, Phys. Rev. B **82**, 195132 (2010).
- [61] G. D. Mahan, *Many-Particle Physics* (Springer US, 2000).
- [62] This is true if the diagrams are defined in terms of the free Green function (excluding the electron-electron term of the Hamiltonian) and the bare interaction or the effective Hubbard  $U$  interaction. We will later use the Kohn-Sham Green function and the fully screened interaction  $W$ , in which case the two diagrams (omitted in the present formulation) would contain double-counting errors in themselves.
- [63]  $R = -2R^{(4)}$  in the notation of Ref. 43.
- [64] To sketch the derivation, which can be found in many textbooks, e.g., Ref. 61, we write Eq. (16) as the sum of two terms corresponding to the cases  $t_1 > t_2$  and  $t_1 < t_2$  with the help of the Heaviside function  $\theta(t_1 - t_2) = 1$  for  $t_1 > t_2$  and 0 otherwise. (It should be noted that, in the fermionic case, the operator  $\mathcal{T}$  is defined to introduce a factor  $-1$  when it switches the field operators.) Then, inserting the closure relation  $\sum_m |\Psi_m^{\sigma\pm}\rangle \langle \Psi_m^{\sigma\pm}| = \hat{1}$  between the two field operators in each term, using  $\hat{\psi}^\sigma(\mathbf{r}t) = e^{i\hat{H}t} \hat{\psi}_S^\sigma(\mathbf{r}) e^{-i\hat{H}t}$  and  $\int \theta(t) e^{i\omega t} dt = i/(\omega + i\eta)$  yields Eq. (17).
- [65] The relatively strong energetic shift results from employing the same parameters  $\Delta_x$  and  $\Delta_v$  as for the full  $GT$  calculations, without readjusting them to the self-energy presently restricted to the third-order diagram.